

NATIONAL INSTITUTE FOR FUSION SCIENCE

New Development of Beam Physics and the
Application by New Generation Pulsed Power
Technology

Edited by Tetsuo Ozaki and Sunao Katsuki

(Received - 2020/04/21)

NIFS-PROC-118

June. 29, 2020

New Development of Beam Physics and the Application by New Generation Pulsed Power Technology

Edited by Tetsuo Ozaki and Sunao Katsuki

January 8-9, 2019
National Institute for Fusion Science
Toki, Gifu, Japan

ABSTRACT

The papers presented at the symposium on “New Development of Beam Physics and the Application by New Generation Pulsed Power Technology” held on January 8-9, 2019 at National Institute of Fusion Science are collected. The papers in this proceeding reflect the current status and progress in the experimental and theoretical researches on high power particle beams, high energy density plasmas produced by pulsed power technology.

Keywords

high power particle beams, high energy density plasma, pulsed power technology, z-pinch, soft x-ray, EUV, neutron source, pulsed discharge, high power microwave, material processing, biological application

All figures and some parts of sentences are in color only CD-ROM(PDF).

Editors' Preface

The symposium entitled “New Development of Beam Physics and the Application by New Generation Pulsed Power Technology” was organized as a part of the General Collaborative Research of National Institute for Fusion Science (NIFS) and held on January 8-9, 2019 at NIFS, Toki.

In the symposium, 32 papers were presented in two days, of which 10 papers are reported in this proceeding. The total number of participants was 48 including students and researchers from universities and companies.

The main objective of the symposium is to provide a place of discussion about the pulsed power technology, generation of plasmas by using pulsed power technology and its application. Therefore, the papers in this proceeding reflect the current status and progress in the experimental and theoretical researches on high power particle beams and high energy density plasmas produced by pulsed power technology in Japan. It is our great pleasure with the unexpectedness if the symposium was beneficial to the development of pulsed power and fusion technologies.

We would like to express our sincere thanks to all of the participants, the authors and the staff of NIFS. This symposium was financially supported by National Institute for Fusion Science budget (NIFS18KKGH031).

Tetsuo Ozaki
National Institute for Fusion Science

Sunao Katsuki
Kumamoto University

Contents

Surface charge measurements via an oblique incidence method with bismuth silicon oxide.	1
Yasuhiro Kamabuchi, Takaharu Kamada, Katsuyuki Takahashi, Seiji Mukaigawa, Koichi Takaki (Iwate University)	
Evaluation of electrical characteristics of 13 kV SiC-MOSFET and development of inductive energy storage pulsed power generator	7
Taichiro Onodera, Katsuyuki Takahashi, Koichi Takaki, and Kunihiro Sakamoto (Iwate University)	
Non-uniformity Mitigation of Fuel Pellet Implosion in Heavy Ion Fusion	13
R. Sato, K. Uchibori, T. Karino, S. Kawata, A. I. Ogoyski (Utsunomiya University)	
Soft X-Ray Radiation from CO₂, N₂ and C₃H₈ Discharges in the Divergent Gas-Puff Z Pinch	17
Keiichi Takasugi, Mineyuki Nishio (Nihon University)	
Spectroscopic measurement of active species generated in streamer discharge on water surface	22
Takuya Hayashi, Souhei Toyoda, Tomokazu Kanna, Takashi Sakugawa (Kumamoto University)	
Comparison of stopping range and blister skin thickness generated by 4 MeV helium ion beam in tungsten.	26
Yuki Uchida, Seiki Saito, Nobuo Saito, Tsuneo Suzuki, Kazumasa Takahashi, Toru Sasaki, Takashi Kikuchi (Nagaoka University of Technology)	
Effect of Electrode Polarity to Atmospheric Pressure Plasma Jet and its Applicability to Surface Modification of Bio-compatible Material.	30
W.T. Leon S. Fernando, Ryo Kobayashi, Kazumasa Takahashi, Takashi Kikuchi, Kiyoshi Ohnuma, and Toru Sasaki (Nagaoka University of Technology)	
AC glow discharge in liquids: the transfer of charged particles and the ability to noble metal nanoparticle synthesis	37
Thai Van Phuoc, S. Abe, K. Kosugi, N. Saito, K. Takahashi, T. Sasaki, and	

T. Kikuchi (Nagaoka University of Technology)

Research on Primary Streamer Propagation Characteristics of Nanosecond Pulsed Discharge in Coaxial Electrode 41

Terumasa Ryu, Hitoshi Yamaguchi, Douyan Wang, and Takao Namihira
(Kumamoto University)

Effect of oxygen concentration on ethylene decomposition by nanosecond pulsed discharge. 47

Yasuaki Torigoe, Asuki Iwasaki, Douyang Wang, Takao Namihira
(Kumamoto University)

Characteristic Investigation of the Pulsed Radiation Generated by Electron Beam Irradiation. 52

Kenji Kashine, Taiki Fujishiro, Yusuke Nakayama, Fumihito Tamura,
Takashi Kikuchi, Weihua Jiang, Akira Tokuchi
(NIT, Kagoshima college)

List of Participants

Koichi Takagi	(Iwate University)
Yasuhiro Kamabuchi	(Iwate University)
Taichiro Onodera	(Iwate University)
Takeshi Kashine	(Institute of Technology Kagoshima)
Akira Tokuchi	(Pulsed Power Japan laboratory)
Jun Hasegawa	(Tokyo Institute of Technology)
Tomoya Usui	(Tokyo Institute of Technology)
Shinnosuke Tabata	(Tokyo Institute of Technology)
Ryo Sato	(Utsunomiya University)
Weihua Jiang	(Nagaoka University of Technology)
Taichi Sugai	(Nagaoka University of Technology)
Ren Xiaojingooa	(Nagaoka University of Technology)
Wataru Kohzu	(Nagaoka University of Technology)
Kiritomo Sato	(Nagaoka University of Technology)
Tsukinosuke Ikemoto	(Nagaoka University of Technology)
Keiichi Takasugi	(Nihon University)
Tohru Kawamura	(Tokyo Institute of Technology)
Takuya Hayashi	(Kumamoto University)
Sunao Katshuki	(Kumamoto University)
Kentaro Kishimoto	(Kumamoto University)
Takashi Kikuchi	(Nagaoka University of Technology)
Yuudai Uchida	(Nagaoka University of Technology)
W.T. Leon S. Fernand	(Nagaoka University of Technology)
Thai Van Phuoc	(Nagaoka University of Technology)
Hironobu Higuchi	(Nagaoka University of Technology)
Hironori Aoyama	(Nagaoka University of Technology)
Hiroaki Ito	(Toyama University)
Fumiya Niwa	(Toyama University)
Masashi Terada	(Toyama University)
Haruyasu Ishida	(Toyama University)
Ryota Tanaka	(Toyama University)
Sho Suzuki	(Toyama University)
Wataru Oyamada	(Toyama University)
Yuuto Sagano	(Toyama University)
Takao Namihira	(Kumamoto University)
Terumasa Ryu	(Kumamoto University)
Yasuaki Torigoe	(Kumamoto University)
Ken Watanabe	(Kumamoto University)
Katsuya Okamura	(KEK)

Tatsuya Kaitou	(KEK)
Yi Liu	(KEK)
Takeshi Higashiguchi	(Utsunomiya University)
Tetsuo Ozaki	(National Institute for Fusion Science)
Yuuji Takemura	(National Institute for Fusion Science)
Shunya Nakamoto	(National Institute for Fusion Science)
Mitsutaka Isobe	(National Institute for Fusion Science)

Surface charge measurements via an oblique incidence method with bismuth silicon oxide

Yasuhiro Kamabuchi, Takaharu Kamada*, Katsuyuki Takahashi,
Seiji Mukaigawa, Koichi Takaki

*The Graduate School of Arts and Science, Iwate University,
4-3-5 Ueda, Morioka, Iwate 020-8551, Japan*

**Department of Industrial Systems Engineering, National Institute of Technology Hachinohe College,
16-1 Uwanotai, Tamonoki, Hachinohe, Aomori 039-1192, Japan*

ABSTRACT

Surface charge measurement using an optical method was achieved by measuring the interference light generated by the Pockels effect for an optical crystal. The interference effect is caused by the phase retardation of output light. The output light intensity that is proportional to the electric field in the crystal was obtained. In this study, we report the measurements on surface charge density distribution based on laser interference under dielectric barrier discharge and the interference effect measurements via oblique incidence laser interferometry using an electro-optical crystal. The charge density distribution was observed at the part corresponding to the filament, and the maximum charge density reached 25 nC/cm². The interference effect was also confirmed to be in the range of the incidence angle from 0° to 60°. Sufficient interference effect was obtained via the oblique incidence laser interferometry.

Keywords

Bismuth silicon oxide, Surface charge, Dielectric barrier discharge, The oblique incidence laser

1. Introduction

In semiconductor manufacturing process, such as plasma processing or ion implantation, charging phenomena on wafers occur and the nonuniformity of charging causes the yield. Hence, measurements of surface charge distribution on wafers are important for evaluating the process quality.

For surface charge measurement, there is an optical method to measure the surface charge using the Pockels effect of an optical crystal. Surface charge measurements via an optical method are resistant to the noise caused by plasma because the charge is calculated from the electric field induced by the accumulated surface charge^[1]. This method also offers advantages of a strong temporal resolution^{[1][2][3]} and minimal disturbance for the sample material^{[1][4][5]}.

In this study, we measured the surface charge density via oblique incidence laser interferometry using the Pockels effect of a Bi₁₂SiO₂₀ (BSO) crystal to measure the charge distribution on a wafer. However, in this experimental system, it is expected that the measurement of surface charge becomes difficult because the output light splits depending on experimental conditions such as applied voltage and the incidence angle of light beam. This paper reports measurements of the surface charge density distribution in dielectric barrier discharge and the interference effect at the oblique incidence of laser.

2. Experimental Setup

2.1 Surface charge measurement using BSO crystal

The discharge cell and charge measurement system are shown in Figure 1 and Figure 2, respectively. The discharge cell was a parallel plate electrode structure composed of dielectrics, spacer, and BSO crystal. A glass plate with a thickness of 530 μm was used for the dielectrics. Indium tin oxide (ITO, resistivity 10 to 20 Ω/cm²) was deposited on the dielectric surface. When the ITO electrode on BSO crystal side was grounded and the other electrode was applied a sinusoidal AC voltage with a frequency of 100 kHz, a discharge was generated between the gaps. A high voltage probe (Tektronix P 6015 A) was used for the applied voltage measurement. A Rogowski coil (Pearson CT 2877) was used for the current measurement, which was recorded with an oscilloscope (Tektronix TDS 3042 B). The BSO crystal thickness was 300 and 700 μm. Helium was used as a working gas and introduced into the gap (gap length and width were 140 μm and 17 mm, respectively). A He–Ne laser with a wavelength of 632.8 nm was used as the light source. In the light receiving section, a semiconductor photodetector (Hamamatsu Photonics C 6386-01) was used for surface charge density measurement, and an ICCD camera was used for charge density distribution measurement.

Surface charge measurement was performed by utilizing the polarization state change of the

transmitted light due to the Pockels effect of the BSO crystal. When an electric field is applied to BSO crystal, birefringence occurs. Moreover, phase retardation occurs in the transmitted light. At that time, the phase retardation, $\Delta\phi$, generated in the transmitted light is expressed as

$$\Delta\phi = \frac{2\pi}{\lambda} n_0^3 \gamma_{41} U_{BSO} \quad (1)$$

Here, λ is light source wavelength, n_0 is refractive index of the crystal ($n_0 = 2.54$), γ_{41} is Pockels coefficient of the crystal ($\gamma_{41} = 5 \text{ pm/V}$), and U_{BSO} is applied voltage. The light intensity, I , measured by the semiconductor photodetector is expressed as

$$I = \frac{I_0}{2} \{1 + \sin(\Delta\phi)\} \quad (2)$$

I_0 is light intensity of laser, I_r is transmitted light intensity when no charge is accumulated on BSO crystal surface (reference intensity), I is transmitted light intensity when charge accumulates on BSO crystal. The surface charge density is expressed as

$$\sigma = (I - I_r) \frac{2}{I_0} \frac{1}{k} \frac{\varepsilon_0 \varepsilon_{BSO}}{a_{BSO}} \quad (3)$$

Here, $k = 2\pi n_0^3 \gamma_{41} / \lambda$. The relative permittivity of BSO crystal is $\varepsilon_{BSO} = 56$, and a_{BSO} is thickness of the crystal. Equation (3) assumes that all electric flux lines induced by electrification charge pass through the crystal; however, electric flux lines that go to the opposite side of the crystal also exist. For that reason, the charge density calculated using equation (3) was estimated to be small. Therefore, the surface charge density was obtained by multiplying equation (3) by a correction coefficient, α , when electric flux lines toward the opposite side of the crystal are concerned. α is 2.12 at the BSO crystal thickness $300 \mu\text{m}$ and 2.16 at $700 \mu\text{m}$. In this experiment, the surface charge density was measured by irradiating the laser beam almost at the center of the discharge area. The diameter of the laser beam was about 1 mm, and the average surface charge in the beam region would be measured.

2.2 Surface charge calculation using discharge current

To verify the accuracy of the charge measured using the BSO crystal, the calculated charge density using the Pockels effect was compared with the calculated surface charge density using the discharge current. The discharge current was obtained by subtracting the displacement current from the measured current waveform based on a previous report by Liu et al. [6]. The transport charge in the half cycle was obtained by time integration of the discharge current. To calculate the surface charge density, the calculated transport charge was divided by the discharge area, S .

2.3 Laser interference measurement using oblique incidence type optical system

Figure 3 shows an interference measurement system. A He-Ne laser with a wavelength of 632.8 nm was

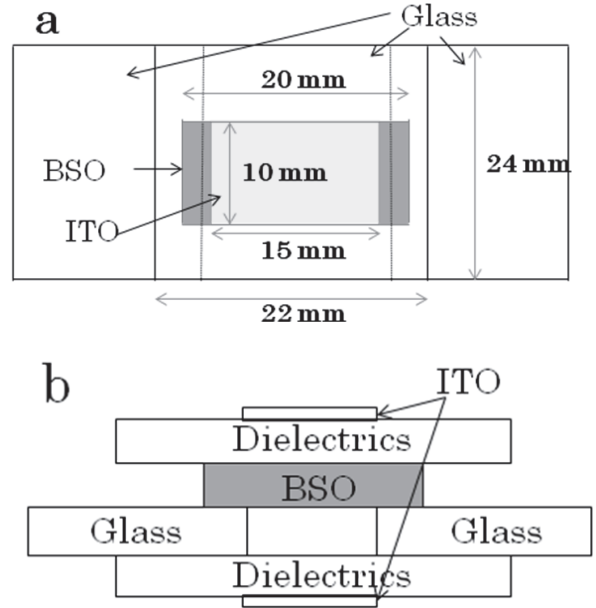


Figure 1. Discharge cell: (a) top view, (b) side view

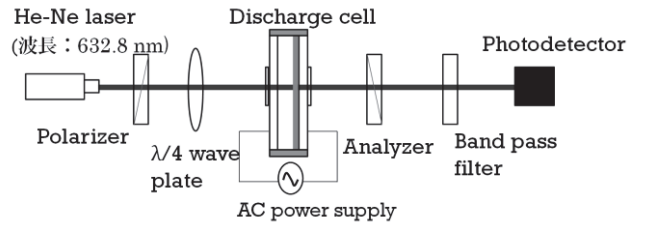


Figure 2. Charge measurement system

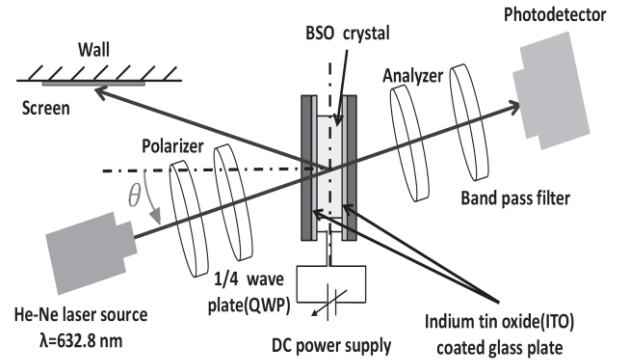


Figure 3. Interference measurement system

used as the light source and the transmitted light intensity was measured using a semiconductor photodetector (Hamamatsu photonics C 6386-01). A BSO crystal with a thickness of $700 \mu\text{m}$ was used as the optical crystal. The BSO crystal was sandwiched between an ITO-coated glass plates. A voltage of 0 to 1000 V was applied using a DC power supply (Max-electronics AMI-5K6P). The incidence polarization state of the crystal was changed by using a polarizer and a quarter-wave plate (QWP). The incidence angle, θ , of the laser beam was estimated from the position of the laser light source, the crystal, and the reflected light

on the screen. To observe the waveform, an oscilloscope (Tektronix DPO 3054) was used. A high voltage probe was used for the applied voltage measurement and a Rogowski coil was used for the current measurement.

3. Results and Discussion

3.1 Surface charge density comparison by crystal thickness difference

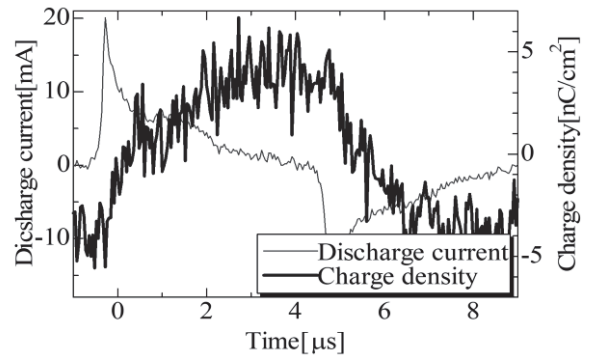
Figure 4 shows the surface charge density and the discharge current. Figures 4 (a) and 4 (b) shows the cases of the crystal with the of $a_{BSO} = 300 \mu\text{m}$ and $a_{BSO} = 700 \mu\text{m}$, respectively. The gas flow velocity was 14.0 m/s, and the maximum discharge current was about 20 mA. The experiments were performed by arranging the amount of electrification charge under glow discharge. The maximum charge density was 4.7 nC/cm^2 at the crystal thickness $a_{BSO} = 300 \mu\text{m}$, and 5.2 nC/cm^2 at $a_{BSO} = 700 \mu\text{m}$. In comparison with this, no large difference in the charge density was found even when the BSO crystal thickness was changed at the time of uniform discharge. In addition, it was found that the states of the transition between discharge current and charge density is consistent with both results. Furthermore, it can be confirmed that the noise was large in the charge waveform of $a_{BSO} = 300 \mu\text{m}$. A possible reason for this noise is the insufficient polarization due to thin crystal and short optical path lengths.

3.2 Surface charge density distribution measurement using BSO crystal

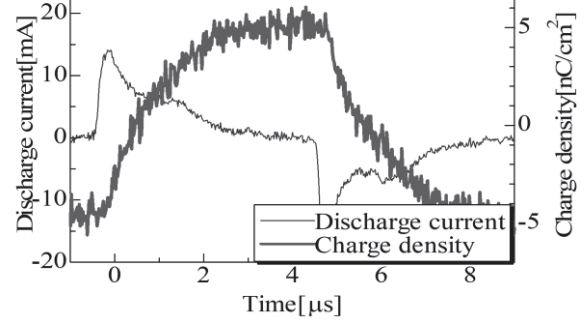
Using a discharge cell with a BSO crystal thickness of $700 \mu\text{m}$, the discharge structure was filamentary under the conditions of gas flow velocity of 7.0 m/s and the maximum discharge current of 6.5 mA. Figure 5 is a discharge image taken with a digital camera, and the frame in the figure was taken as the measurement area.

Figure 6 and Figure 7 show the luminance value of the reference intensity, I_r , and the transmitted light intensity, I , obtained from the ICCD camera, respectively. Figure 8 shows the charge density distributions obtained from Figure 6, Figure 7, and equation (3). It can be seen that the portion where the filament appeared and the portion where a higher charge density was found substantially coincided. However, a high charge density can also be confirmed in the part without filament.

Next, the discharge area calculated from the discharge images was compared with the one calculated from the V-Q Lissajous figure. The discharge area, S , was calculated as 0.131 cm^2 from the discharge images because the number of filaments was 24 and the diameter of each filament was 0.083 cm . Figure 9 shows the applied voltage and the electrification



(a) BSO crystal thickness $a_{BSO} = 300 \mu\text{m}$



(b) BSO crystal thickness $a_{BSO} = 700 \mu\text{m}$

Figure 4. Variation of Surface charge density with discharge current

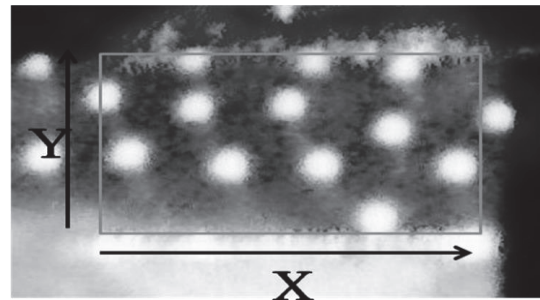


Figure 5. Discharge image (digital camera)

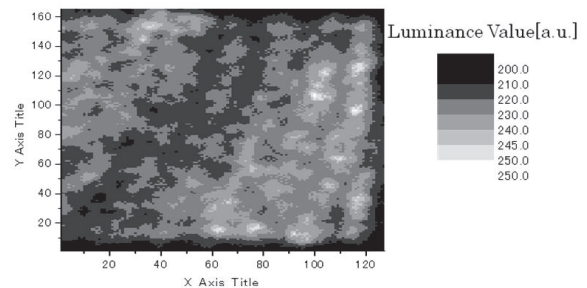


Figure 6. Luminance value of I_r

charge during the filamentary discharge. From the V-Q Lissajous figure, the reactor capacity at the time of discharge was calculated and the discharge area was calculated to be 1.24 cm^2 . From this, the discharge area calculated using the V-Q Lissajous figure is larger than the one based on discharging images. Therefore, it is

considered that the discharge occurred even in the part where the filament was not clearly visible by visual observation. In the surface distribution measurement by the BSO crystal, it was found that the discharge occurred even in a portion where the filament did not exist, and electric charge accumulated.

From Figure 8, the maximum charge density calculated using the BSO crystal was 25 nC/cm^2 . Because the maximum charge of 4.2 nC was deposited on the crystal surface (Figure 9), the charge density was calculated to be 32 nC/cm^2 . The comparison of the calculated results shows that the charge density is almost the same.

3.3 Laser interference measurement at oblique incidence of light

Figure 10 shows the change in the intensity of the transmitted light when the applied voltage was kept constant at 500 V and the optical elements were rotated. When no crystal was inserted into the optical system and the optic axes of the polarizer and the analyzer were orthogonal to each other, the transmitted light was not observed. However, when the crystal was inserted, the transmitted light was generated due to the Pockels effect, which showed a sinusoidal change at the time of crystal rotation. Similarly, when the light was made incident at an angle of incidence, θ , regarding the crystal, the light showed a sinusoidal change. Moreover, in the waveform when the QWP was not inserted, the maximum light intensity value and the optical elements rotation angle at that time is different. Due to the oblique incidence of the light beam, there is a change of the incidence polarization state. For that reason, it can be said that the insertion of a QWP is desirable for constructing the interferometry.

Figure 11 shows the transmitted light intensity characteristics as a function of the applied voltage. According to the theoretical equation (2) of the Pockels effect, the phase shift of the transmitted light intensity is proportional to the applied voltage, U_{BSO} , on the crystal. Even when the laser light was at an oblique incidence, the tendency of the intensity change is different. However, the same change is confirmed. Therefore, the interference effect was confirmed when the incidence angle was in the range of approximately 0° to 60° .

3.4 Changing rate of transmitted light intensity per applied voltage of 1 V

The change rate of the transmitted light intensity per applied voltage of 1 V was obtained from the intensity value of Figure 11 and compared with the theoretical calculation. Figure 12 shows the catadioptric model used for the theoretical calculation where the phase retardation at oblique incidence is calculated from the difference in optical path lengths by considering Snell's law on the crystal surface. The change rate was

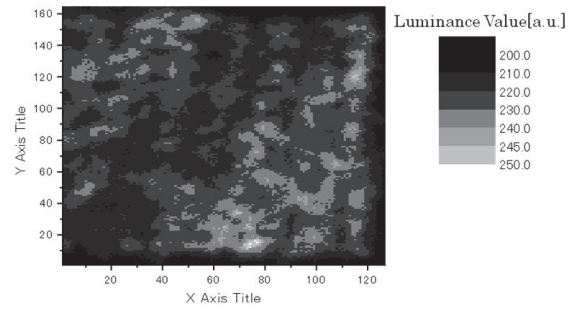


Figure 7. Luminance value of I

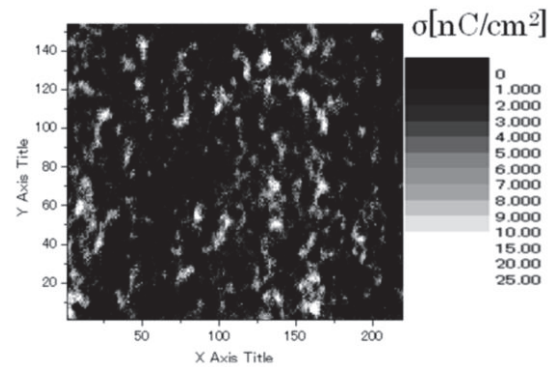


Figure 8. Charge density distribution

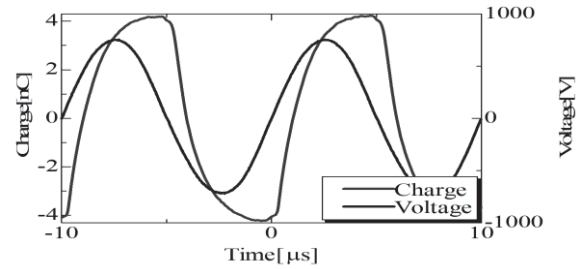


Figure 9. Applied voltage and electrification charge

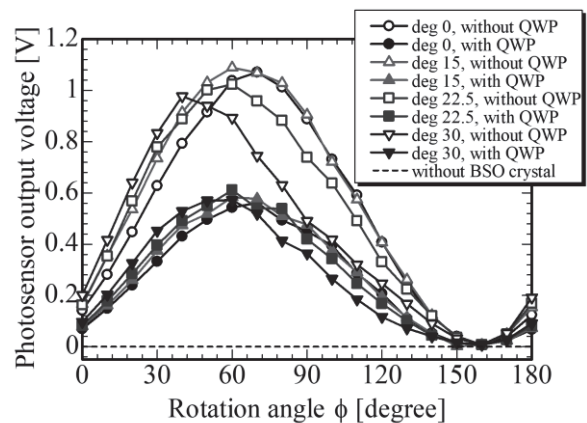


Figure 10. Light intensity changes during rotation of the optical elements

obtained by substituting the phase retardation at oblique incidence into equation (2). When an external electric field, E , is applied to the crystal and the light is obliquely incidence, the phase retardation in the

transmitted light is express as

$$\Delta\phi = \frac{2\pi}{\lambda} a_{BSO} \left(\frac{N_1}{\cos \beta_1} - \frac{N_2}{\cos \beta_2} \right), \beta_i = \sin^{-1} \left(\frac{\sin \theta}{N_i} \right)$$

Here, N_1 and N_2 are refractive indices for the respective polarizations, which are indicated by $N_1 = n_0 - (n_0^3 \gamma_{41} E/2)$ and $N_2 = n_0 + (n_0^3 \gamma_{41} E/2)$.

Figure 13 shows the change rate of the transmitted light intensity per applied voltage of 1 V. In the experimental value, the change rate is $6.1 \times 10^{-5} \%$ /V at the incidence angle of 0° and $8.9 \times 10^{-5} \%$ /V at 62.5° . Even when the incidence angle was changed, the change rate did not change greatly. Therefore, a sufficient interference effect can be obtained also via the oblique incidence laser interferometry. The calculated value is $8.14 \times 10^{-4} \%$ /V at the incidence angle of 0° and $7.48 \times 10^{-4} \%$ /V at 62.5° . The decreasing tendency by increasing the incidence angle is confirmed. In addition, about 10 times difference was confirmed between the experimental value and the calculated value. However, it is thought to be related to the facts that experiments cannot be performed under ideal conditions yet and that theoretical calculation did not include natural birefringence [7].

4. Conclusions

We measured the surface charge density based on laser interference under dielectric barrier discharge and the transmitted light intensity at the time of rotation of the optical elements and the change in the applied voltage using an oblique incidence optical system.

In the surface charge density distribution, a signal corresponding to the filament was observed, and the maximum surface charge density reached 25 nC/cm^2 .

The interference effect was confirmed when the incidence angle was in the range of approximately 0° to 60° .

A sufficient interference effect can also be obtained via oblique incidence laser interferometry since the change rate is $6.1 \times 10^{-5} \%$ /V at the incidence angle 0° and $8.9 \times 10^{-5} \%$ /V at 62.5° .

Reference

- [1] L. Stollenwerk, "Interaction of current filaments in dielectric barrier discharges with relation to surface charge distributions", *New Journal of Physics*, Vol. 11, 103034 (2009)
- [2] N. Takeuchi, T. Hamasaki, K. Yasuoka, T. Sakurai, "Surface charge measurement in surface dielectric barrier discharge by laser polarimetry", *J. Electrostatics*, Vol. 69 (2011) PP.87-91
- [3] D. C. Jeong, H. S. Bae, and K. W. Whang, "Measurement of the spatiotemporal surface charge distribution in an ac plasma display cell using Pockels effect", *J. Appl. Phys.*, Vol. 97, 013304 (2005)
- [4] L. Stollenwerk, J. G. Laven, and H. -G. Purwins, "Spatially Resolved Surface-Charge Measurement in a Planar Dielectric-Barrier Discharge System", *Phys. Rev. Lett.*, 255001 (2007) PP.1-4

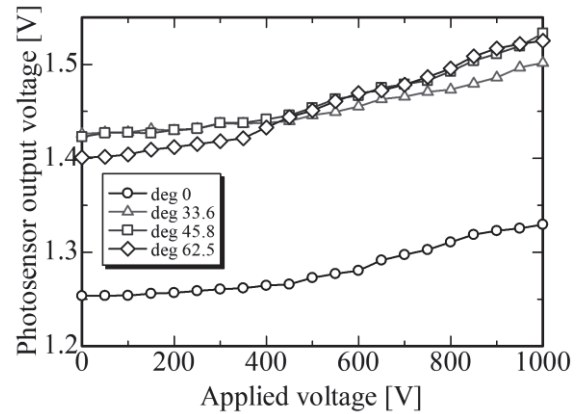


Figure 11. Transmitted light intensity as a function of applied voltage

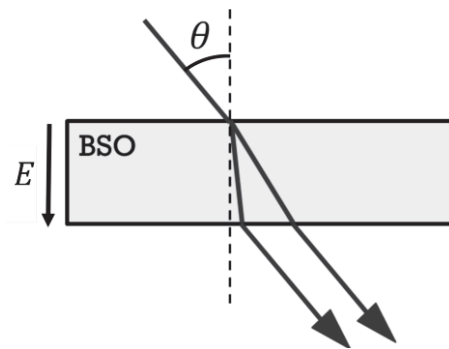


Figure 12. Catadioptric model

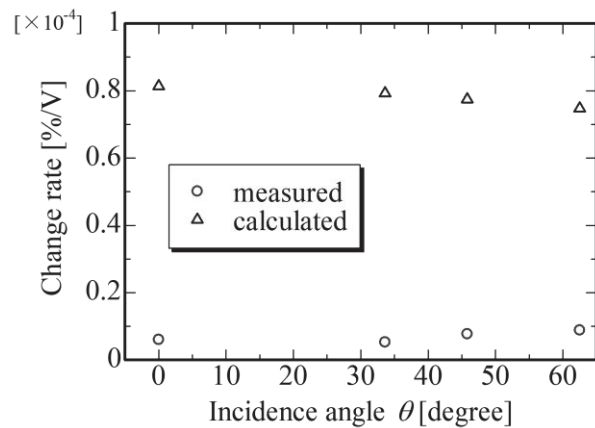


Figure 13. Changing rate of transmitted light intensity per applied voltage of 1 V

- [5] F. Gegot, Th. Callegari, M. Aillerie, and J. P. Boeuf, "Experimental protocol and critical assessment of the Pockels method for the measurement of surface charging in a dielectric barrier discharge", *J. Phys. D*, Vol. 41, 135204 (2008)
- [6] S. Liu, M. Neiger, "Electrical modelling of homogeneous dielectric barrier discharges under an arbitrary excitation voltage", *J. Phys. D*, Vol. 36 (2003) 3144

[7] P. Pellet-Finet, "Measurement of the electro-optic coefficient of BSO crystal", *Opt. Commun*, Vol. 50 (1984) PP. 275-280

Evaluation of electrical characteristics of 13 kV SiC-MOSFET and development of inductive energy storage pulsed power generator

Taichiro Onodera, Katsuyuki Takahashi, Koichi Takaki, and Kunihiro Sakamoto*

Iwate University

**National Institute of Advanced Industrial Science and Technology,*

ABSTRACT

Electrical characteristics of a silicon carbide (SiC)-MOSFET with blocking voltage of 13 kV were evaluated and inductive energy storage (IES) pulsed power generator was developed. The experiment to evaluate was carried out using a circuit which consists of a capacitor and a resistor. The maximum pulsed current of 118 A, the fall time of stabilized at 40 ns at a large current more than 30 A, on-resistance 0.86 Ω were obtained. The IES pulsed power generator consisted of the SiC-MOSFET employed as opening switch, a capacitor, and a pulsed transformer. The maximum output of 31.4 kV and full width at half maximum of 55 ns were obtained with an input voltage of 1100 V and a charging time of 500 ns. The output pulse energy was 8.6 mJ corresponding to 50.2 % of the input energy with a load resistance 2.5 k Ω .

Keywords

Pulsed power, Silicon carbide, MOSFET

1. Introduction

Plasma application technology by high-voltage pulsed discharge is attracting attention for the removal of environmental pollutants such as nitrogen oxides (NOx) and organic compound^{[1][2]}. Pulse discharge develops in two main phases; streamer corona discharge propagation phase and glow-like discharge. When a high positive voltage is applied to a center electrode (i.e., anode), a small luminous zone called a streamer head, develops from the center electrode to the outer electrode (i.e., cathode). The streamer head reaches the cathode and generates an ionized filament that bridges the gap between the anode and cathode. This initial phase of streamer propagation is called the “primary streamer”. After the arrival of the primary streamer at the cathode, a subsequent streamer develops from the anode toward the cathode, is called a “secondary streamer” or a “glow-like discharge”. The characteristics of the primary and secondary

streamers are quite different. The primary streamer includes a relatively large number of high-energy electrons to dissociate molecules such as oxygen and nitrogen with high efficiency^[3]. To inhibit the transition to glow-like discharge, the pulsed power generator simultaneously realizes a high-voltage output and a short pulse generation time is required^[4].

Conventional triggers mounted on pulsed power generator have been used spark gap switches utilizing dielectric breakdown of air. However, it is difficult to implement in application fields because it has switch deterioration and operation instability. In order to solve this problem, researches are being carried out to apply semiconductor power devices having a semi-permanent lifespan and easy to control to triggers^[5]. Although current semiconductor power devices, such as IGBT, with high-voltage and high-current handling capacities can obtain high output energy, its switching time is slow.

MOSFET is a kind of semiconductor, it is a relatively small capacity and high-speed device. Previously, further improvement in that capacity was achieved by devising the structure^[6]. However, realization of further performance is extremely difficult based on the physical properties of the conventional Silicon (Si) material. Silicon carbide (SiC) has attracting attention as a high-performance material replacing Si. SiC is known to have a bandgap of about 3 times, a dielectric breakdown electric field of about 10 times and a thermal conductivity of about 3 times higher than that of Si. There are shown that has high-temperature operation, low loss characteristics and high exhaust heat respectively^{[7][8]}.

In this research, the characteristics of SiC-MOSFET developed by Tsukuba Power Electronics Constellations (TPEC) with blocking voltage 13 kV^[9] is evaluated to develop a pulsed power generator capable of realizing both high output voltage and ultra-short pulses. The characteristics of the inductive energy storage (IES) pulsed power generator using the SiC-MOSFET as switching device are also evaluated.

2. Experimental Setup

Figure 1 shows the schematics of evaluation circuit for the switching characteristics. Capacitive energy is stored in the capacitor of the capacitance C_B via the resistor R of 500 k Ω from the DC stabilized power supply V_{DD} . When the pulsed signal from a gate driver is applied between gate and source of the MOSFET, the MOSFET is turned on and the energy stored in the C_B is discharged through the resistor R_L . The drain-source voltage v_{DS} is measured using the voltage probe (Tektronix, P6015A) and the i_D is measured using a current transformer (Bergoz, CT-D1.0-B).

Figure 2 shows the schematics of evaluation circuit for on-resistance of MOS-FET. The circuit consists of two MOSFETs connected in series. The drain of the lower MOSFET (M2) is connected to the source of the upper MOSFET (M1), and the source is grounded. A gate driver is connected to the gate of M1 and DC 20 V is applied to the gate of M2. In order to calculate time change of the on-resistance $r_{DS(ON)}$, when M1 is switched, the v_{DS} ($v_{DS(ON)}$) is measured using the

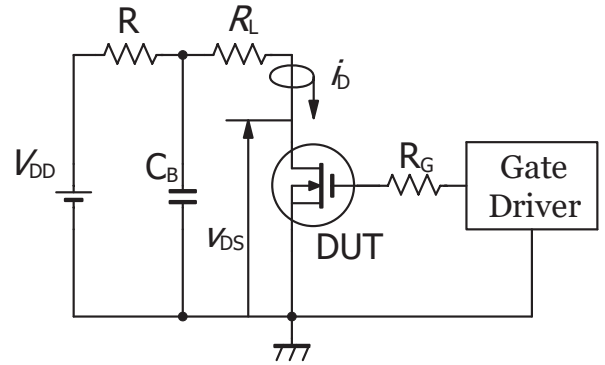


Fig. 1 Schematics of evaluation circuit for switching characteristics.

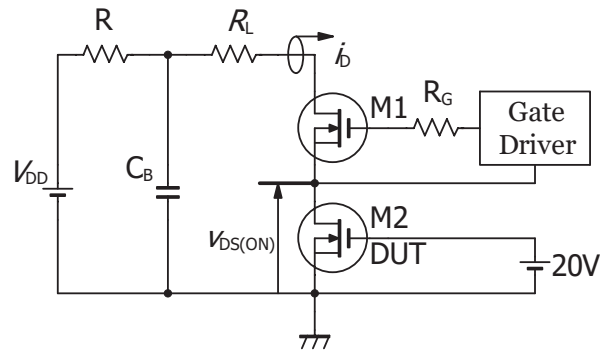


Fig. 2 Schematics of evaluation circuit for on-resistance characteristics.

voltage probe (Tektronix, TPP1000) and the i_D was measured using a current transformer (Bergoz, CT-D1.0-B). The C_B was 0.22 μF , the R_G was 510 Ω , and the pulsed width of the signal was 20 μs .

3. Results and Discussion

3.1 Switching characteristics

Figure 3 shows the waveform of i_D as for various V_{DD} . R_L is shortened. The C_B is 3.3 mF, the gate resistance R_G is 100 Ω , and the pulsed width of the signal is 50 μs . The peak value of i_D increases with increasing V_{DD} . When V_{DD} was 400 V, it has saturated at 155 A without failure.

Figure 4 shows the waveforms of v_{DS} and i_D when the MOS-FET is turned on and off. The C_B was 0.22 μF and the pulsed width of the signal was 250 ns. The V_{DD} is 10 kV and R_L is 500 Ω . The time required to reach from 90 % to 10 % at turn-on of v_{DS} is defined as rise time, and 10 % to 90 % at turn-off of v_{DS} is defined as fall time. The rise time and the fall time are 53 ns and 51 ns, respectively, under this condition.

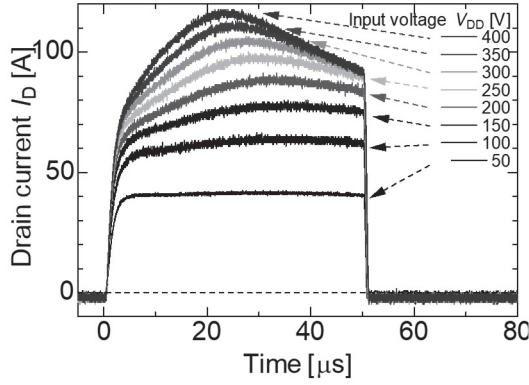


Fig. 3 Waveforms of drain current for various Input voltage.

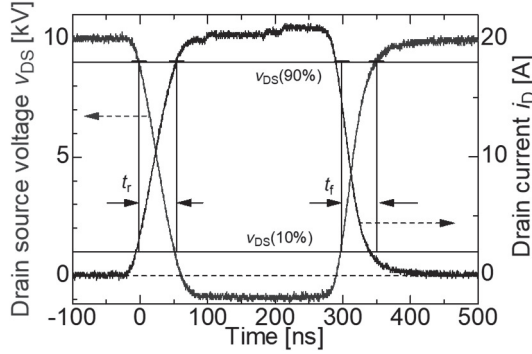


Fig. 4 Waveforms of drain-source voltage and drain current.

Figure 5 shows the rise time and the fall time as a function of R_L and i_D with V_{DD} of 10 kV. The rise time increases with increasing the R_L ; on the other hands, the fall time decreases. When the i_D is higher than 30 A, the fall time has a constant value and is 40 ns. The switching time is about one order faster than a large capacity device such as IGBTs^[10]. Since the drain-source stray capacitance of the drift region is charged through R_L , the fall time of the MOSFET depends on the R_L . Therefore, the MOS-FET is suitable for the large cut-off current in a short time with heavy loading.

3.2 On-resistance characteristics

Figure 6 shows the waveforms of $v_{DS(ON)}$, i_D and $r_{DS(ON)}$ calculated from $v_{DS(ON)}$ and i_D . The values of V_{DD} and R_L are 10 kV and 990 Ω , respectively. Because the resolution of the measurement system is not enough, $r_{DS(ON)}$ is not calculated at the off-state of switching. The value of $r_{DS(ON)}$ at the time when the

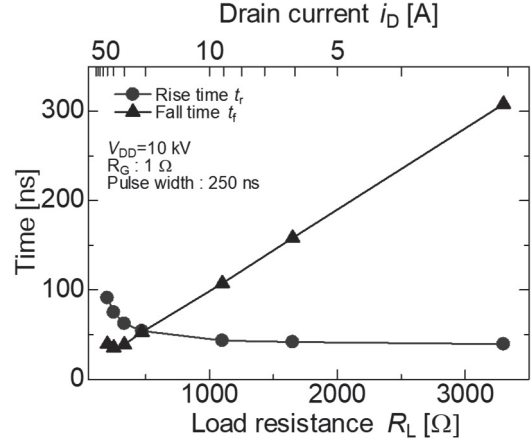


Fig. 5 Rise and fall times as a function of load resistance.

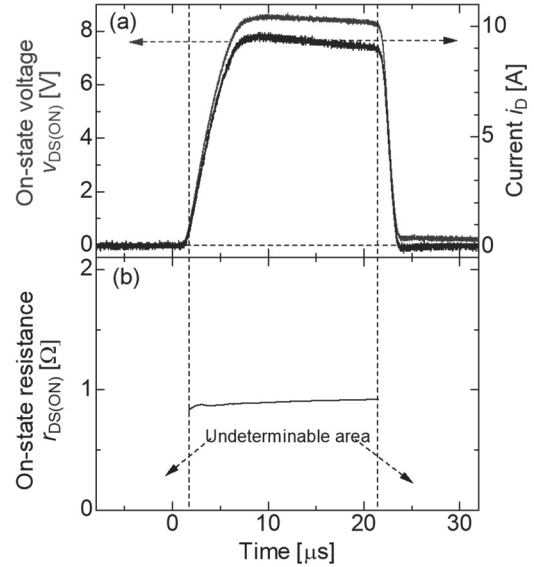


Fig. 6 Waveforms of (a) Drain-source voltage and drain current (b) calculated time change the on-resistance.

calculation was started was 0.86 Ω .

Figure 7 shows the $r_{DS(ON)}$ as a function of input voltage and current. The $r_{DS(ON)}$ is independent of input voltage and current. From this, it can be seen that low loss is expected in the on-state and easy to loss calculation.

4. IES pulsed power generator

The electrical characteristics show that the device is suitable for an opening switch because its low on

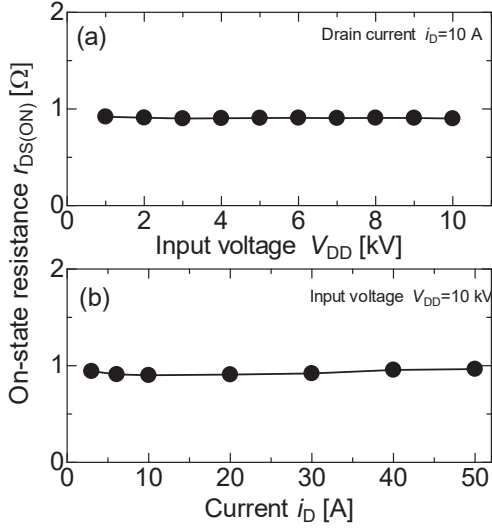


Fig. 7 On-resistance as a function of (a) Input voltage (b) current.

resistance and rapid current cut-off. In this study, an inductive energy storage (IES) pulsed power generator using the device as an opening switch is developed. Figure 8 shows the schematics of the IES pulsed power generator. The primary circuit consists of energy storage capacitor C_B , a transformer and SiC-MOSFET. The C_B was using 12 μF . The transformer consists of a magnetic core (Hitachi Metals, FT-3H, cross section area $2.6 \times 10^3 \text{ mm}^2$, magnetic path length $3.2 \times 10^3 \text{ mm}$) with the turn ratio 5:15. AC/DC converter and a rectifier is used to reset the transfer with continuous current. During the SiC-MOSFET switch is closed, the charge stored in the capacitor flows through the transformer and MOS-FET, and the inductive energy is stored in the inductance of the pulse transformer. When the MOS-FET switch is opened, the current interrupted. As the results, pulsed voltage appears at the secondary circuit of the transformer.

Figure 9 shows the waveforms of the current flows the primary circuit i_C , v_{DS} , the voltage across the primary transformer v_{L1} , the output voltage of secondary transformer. i_C and output current i_O are measured using a current transformer (bergoz, CT-D1.0-B), v_{DS} , v_{L1} and v_O are measured using voltage probes (Tektronix, P6015A, Testec, TT-SI 9010 and Tektronix, P6015A respectively.) The V_{DD} is 10 kV, a

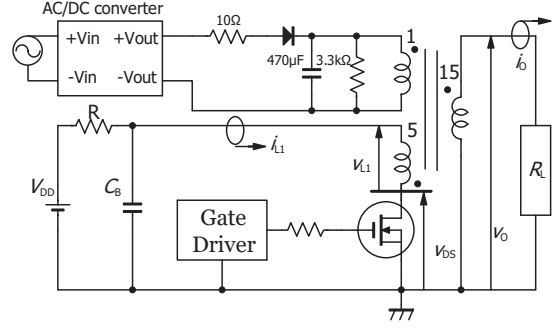


Fig. 8 Schematics of inductive energy storage pulsed power generator using SiC-MOSFET.

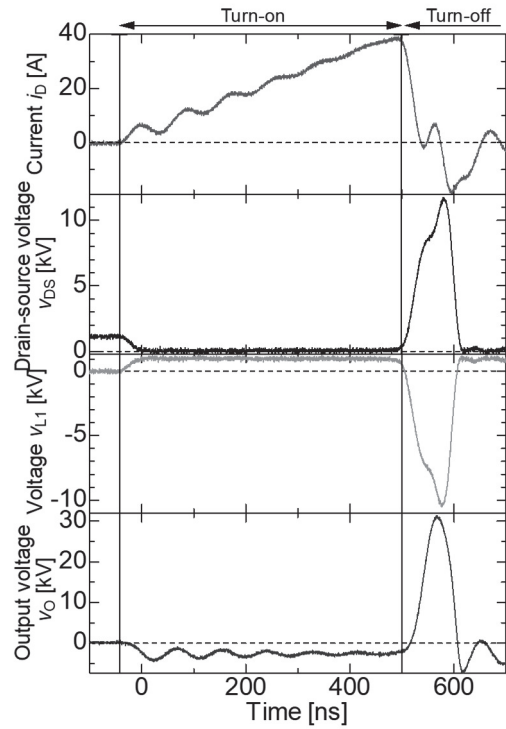


Fig. 9 Waveforms of the current flows the primary circuit i_{L1} , v_{DS} , the voltage across the primary transformer v_{L1} , the output voltage of secondary transformer.

charging time is 500 ns and the R_G is 1 Ω . The i_C has the maximum value of 39 A and is interrupted with the fall time of 27 ns. The maximum value of the v_{DS} and v_{L1} are 11.7 kV and 10.5 kV respectively. The full width at half maximum (FWHM) of v_{DS} and v_{L1} are both 69 ns and 66 ns. The maximum value of v_O is 31.4 kV. FWHM of v_O is increased to 55ns by damping after cutting off the current of i_C .

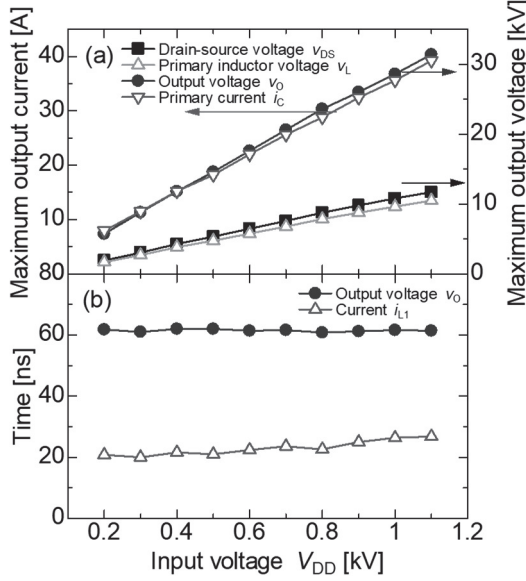


Fig. 10 (a) The maximum values of i_{L1} , v_{DS} , v_L and v_O , and (b) fall time of i_{L1} and FWHM of v_O , as a function of V_{DD} .

Figure 10 shows (a) the maximum values of i_{L1} , v_{DS} , v_L and v_O , and (b) fall time of i_{L1} and FWHM of v_O , as a function of V_{DD} . The maximum value of them are increases with increasing V_{DD} . When V_{DD} is 1100 V, the maximum values of i_{L1} , v_{DS} and v_O are 39 A, 11.7 kV, 31.4 kV respectively. The FWHM of v_O is 55 ns, which was almost constant regardless of the increase in V_{DD} .

Figure 11 shows the energy consumed u_1 in the primary circuit and that u_O in R_L , and the transfer efficiency to output side, as a function of R_L . u_1 is calculated by integrating electric power obtained by the voltage across the C_B and i_{L1} over time. u_O is calculated by integrating the electric power obtained by the v_O and i_O over time. u_O is divided into a charging period, $u_{O(ON)}$, and after current interrupt, $u_{O(OFF)}$. $u_{O(ON)}$ decreases with increasing R_L because the impedance of secondary side of transformer increases. The $u_{O(OFF)}$ has a maximum value, 8.6 mJ corresponding to 50.2 % of the input energy with a load resistance 2.5 k Ω , when R_L is 2.5 k Ω because the impedance of primary and secondary sides after current interrupt is matched.

5. Conclusions

In this research, the electrical characteristics of SiC-

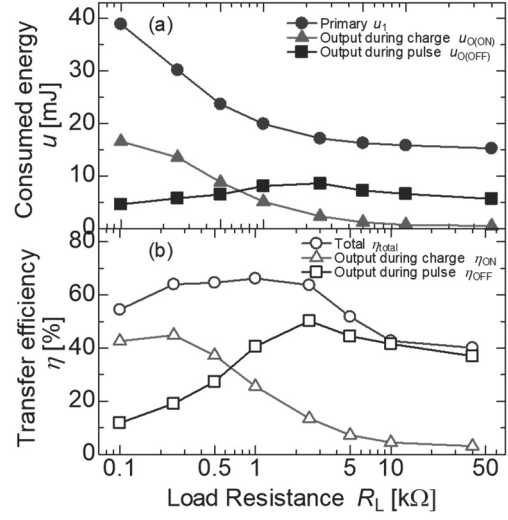


Fig. 11. As a function of load resistance, (a) energy consumption on primary side and output side, and (b) energy transfer efficiency to output side.

MOSFET is evaluated and IES pulsed power generator using SiC-MOSFET is developed. This device can be conducted a large pulsed current of 155 A. Also, fall time is as short as 40 ns with large pulsed current. The on-resistance is 0.86 Ω . The maximum output voltage and FWHM of The IES pulsed power generator are 31.4 kV and 55 ns, respectively. The output pulse energy was 8.6 mJ corresponding to 50.2 % of the input energy with a load resistance 2.5 k Ω .

Acknowledgments

Part of work this work has implemented under a joint research project of Tsukuba Power Electronics Constellations (TPEC).

References

- [1] T. Namihira et al., "Improvement of NOx Removal Efficiency Using Short-Width Pulsed Power", *IEEE Trans. Plasma Sci.*, **28**, 2, pp.434-442 (2000)
- [2] M. A. Malik et al., "Water purification by electrical discharges", *Plasma Sources Sci. Technol.*, **10**, 1, pp.82-91 (2001)
- [3] Y. Teramoto et al., "Streamer Propagation of

- Positive and Negative Pulsed Corona Discharges in Air”, *IEEE Trans. on Plasma Sci.*, **39**, 11, pp.2218-2219 (2011)
- [4] D. Wang et al., “Development of higher Yield Ozonizer Based on Nano-Seconds Pulsed Discharge”, *ISSN J. Adv. Oxid. Technol.*, **13**, 1, pp.71-78 (2010)
- [5] D. Gerber et al., “Gate Unit With Improved Short-Circuit Detection and Turn-off Capability for 4.5-kV Press-Pack IGBTs Operated at 4-kA Pulse Current”, *IEEE Trans. on Plasma Sci.*, **41**, 10, pp.2641-2648 (2013)
- [6] B. J. Baliga, “A new vertical power MOSFET structure with extremely reduced on-resistance”, *IEEE Trans. Electron Devices*, **38**, pp.1568-1575 (1991)
- [7] B. J. Baliga, “Power Semiconductor Device Figure of Merit for High-Frequency Applications”, *IEEE Electron Device Lett.*, **10**, 10 pp.455-457 (1989)
- [8] H. Okumura, “Present status and Future Widegap semiconductor High-Power Devices”, *Jpn. J. Appl. Phys.*, **45**, 10A, pp.7565-7586 (2006)
- [9] H. Kitai et al, “Low on-resistance and fast switching of 13-kV SiC MOSFETs with optimized junction field-effect transistor region”, *2017 29th International Symposium on Power Semiconductor Devices and IC's (ISPSD)*, pp. 343-346, (2017)
- [10] D. Gerber et al., “Gate Unit With Improved Short-Circuit Detection and Turn-Off Capability for 4.5 kV Press-Pack IGBTs operated at 4-kA Pulse Current”, *IEEE Trans. on Plasma Sci.*, **41**, 10, pp.2641-2648 (2013)

Non-uniformity Mitigation of Fuel Pellet Implosion in Heavy Ion Fusion

R. Sato, K. Uchibori, T. Karino, S. Kawata, A. I. Ogoyski¹

Graduate School of Engineering, Utsunomiya University, Utsunomiya, Yohtoh 7-1-2, Utsunomiya 321-8585, Japan

¹Department of Physics, Varna Technical University, Varna 9010, Bulgaria

ABSTRACT

In order to realize inertial confinement fusion, a sufficient energy gain is required. A uniform fuel implosion is essentially required to release the fusion energy. For the uniform implosion, the non-uniformity of the implosion acceleration should be less than a few %. In this research, we propose to employ wobbling heavy ion beams (HIBs) to reduce the HIB illumination non-uniformity and the Rayleigh-Taylor instability growth. The 2-dimensional hydrodynamic computer simulation results demonstrate that the uniform implosion is realized by the wobbling HIBs successfully. In this paper, we present the results for the HIBs wobbling frequency effect on the target gain, and also the results for an HIB illumination timing error on the target gain.

Keywords

Key Words: Implosion, heavy ion beam, inertial confinement fusion

1. Introduction

In inertial confinement fusion, the fusion fuel compression is essentially important to reduce an input driver energy [1, 2]. In order to realize an inertial confinement fusion (ICF) system, a sufficient fusion energy gain is required, and a uniform fuel implosion is required to release the fusion output energy. For the uniform implosion, the non-uniformity of the implosion acceleration should be less than a few % [3, 4]. On the other hand, a dynamic stabilization of plasma instabilities including the dynamic smoothing of plasma non-uniformities was proposed in Refs. [5-9]. In this paper, the dynamic smoothing method is applied to a spherical DT fuel target implosion in heavy ion inertial fusion (HIF), and two-dimensional fluid simulations are performed to investigate the dynamic smoothing effect on the implosion uniformity of the DT fuel spherical pellet, illuminated by heavy ion beams (HIBs). In our study, each HIB axis is oscillated with a high frequency, for example, a few hundred MHz or higher in order to realize the dynamic smoothing [5-9]. We found that the oscillating or wobbling motion of each HIB axis induces a phase-controlled HIBs energy deposition, and consequently the phase-controlled implosion acceleration is realized, so that the HIBs illumination non-uniformity is successfully mitigated. The HIB accelerators provide a well-

established capability to oscillate a HIB axis with a high frequency. The results presented in this paper also demonstrate that the wobbling HIBs would provide an improvement in the fusion energy output gain.

2. Spiral wobbling beam

The oscillating non-uniform acceleration field is obtained by the HIBs' axes oscillation. We used the heavy ion wobbling beams as the irradiation beams onto a DT fuel target. Figure 1 shows a schematic diagram for the spiral wobbling beam. For the spiral wobbling beam, the beam radius changes from 3.8mm to 3.7mm at $1.3\tau_{wb}$.

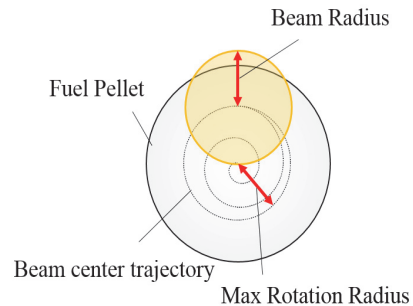


Fig. 1. Schematic diagram for the spiral wobbling beam. The beam center moves spirally until rotation radius becomes 0.9mm.

Here τ_{wb} is the time for one rotation of the wobbling beam axis. The beam rotation radius becomes 0.9mm at $t = 2.0\tau_{wb}$. After that, the beam rotation radius is 0.9mm. When we employ the spiral motion of each HIB axis, the initial imprint of the HIBs illumination non-uniformity is significantly reduced.

3. Fuel pellet implosion

Figures 2 show (a) the HIB input pulse and (b) the DT fuel target structure. The peak power of the foot pulse is 22TW with the initial rising time of 5ns, and the main pulse rises at 8ns and reaches 400TW at 13ns with the 5ns rising and falling

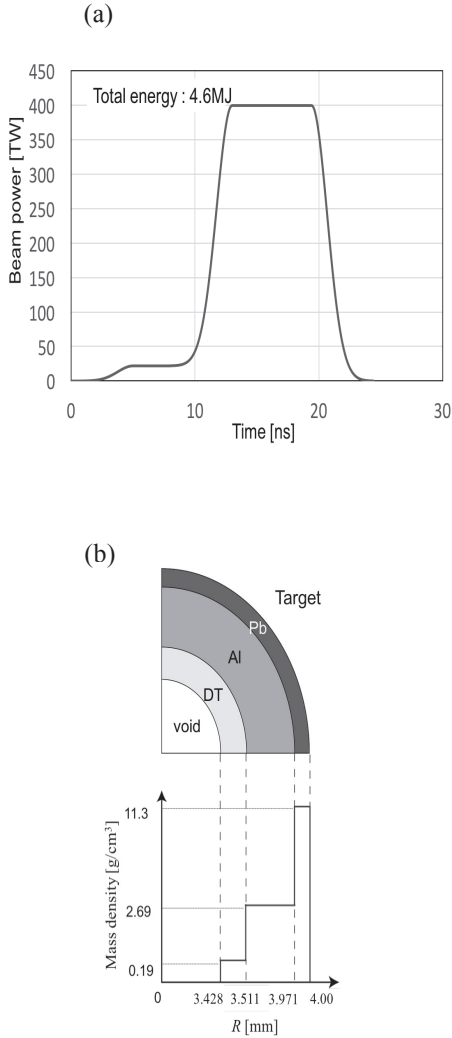


Fig. 2. (a) Input HIB pulse. The HIB pulse consists of the foot pulse and the main pulse. (b) DT fuel pellet structure employed in this paper. The DT total mass is 2.4mg.

times. The HIBs irradiation is terminated at 25.9ns, and the total input energy is 4.6MJ. The spiral trajectory in Fig. 1 is also adopted into the main pulse; for reducing the initial imprint of the HIBs irradiation nonuniformity due to the pulse power rising while the beam wobbling, the same HIB spiral trajectory in Fig. 1 starts again at 10.5ns. The Pb+ beam particle energy is 8GeV. The total HIBs number is 32 [10].

Figures 3 show the fuel target implosion results: Figures 3(a) present the ion temperature

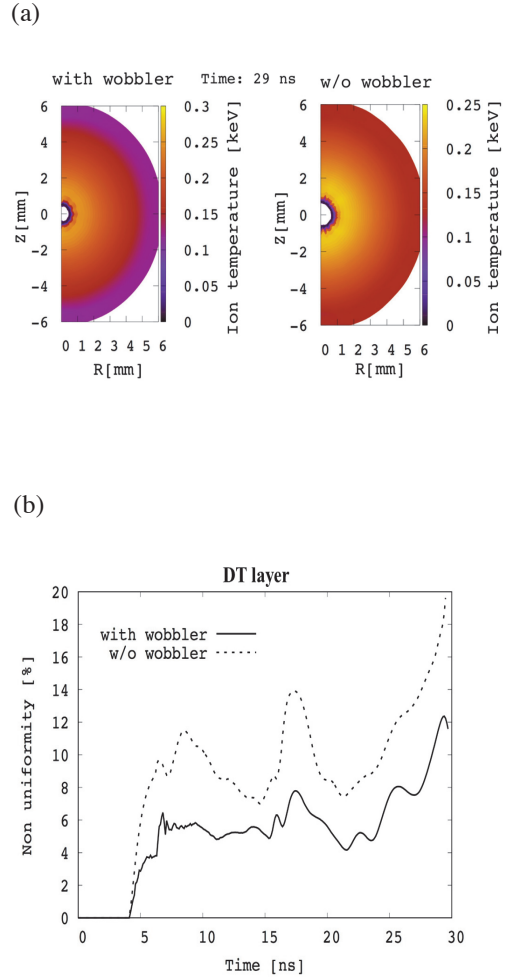


Fig. 3. Implosion results of the fuel target ion temperature. (a) Ion temperature distributions at $t=29$ ns before the void closure with the spiral wobbling beam (left) and without the wobbling beam (right). (b) The RMS nonuniformity histories of the DT ion temperature with the spiral wobbling beam (the solid line) and without the wobbler (the dotted line).

distributions at 29 ns with and without the wobbling motions of HIBs. Figures 3(b) also demonstrate that the HIBs illumination non-uniformity is reduced by the HIBs wobbling motion. Figure 4 shows the fusion energy vs the wobbling rotational frequency. The wobbling HIBs may contribute the HIBs illumination uniformity and may also improve the fusion output energy gain.

In addition, we also examine a HIB illumination timing error on the fusion gain (see Fig. 5). In general, a HIB accelerator may introduce a beam illumination timing error, which may induce a degradation of the fusion energy gain.

In Fig. 6 the DT non-uniformity histories are shown. One HIB's illumination timing error introduces the overall HIBs illumination non-

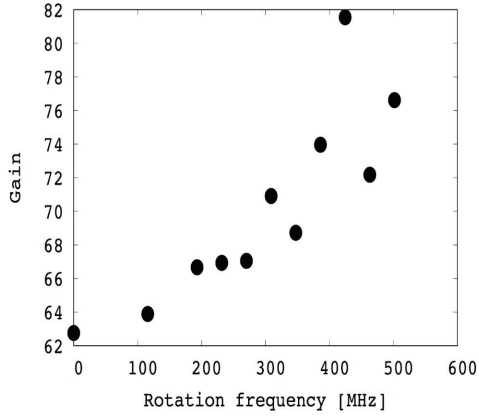


Fig. 4. Energy gain vs the wobbling frequency of the beam axis.

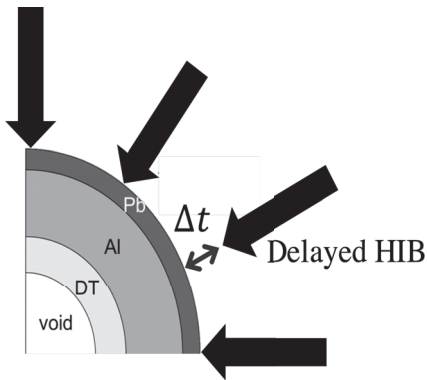


Fig. 5 In a HIF accelerator a HIB may have an illumination timing error, which may induce a degradation of the fusion gain.

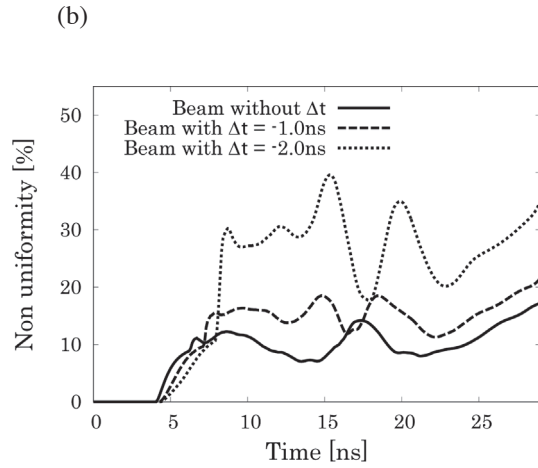
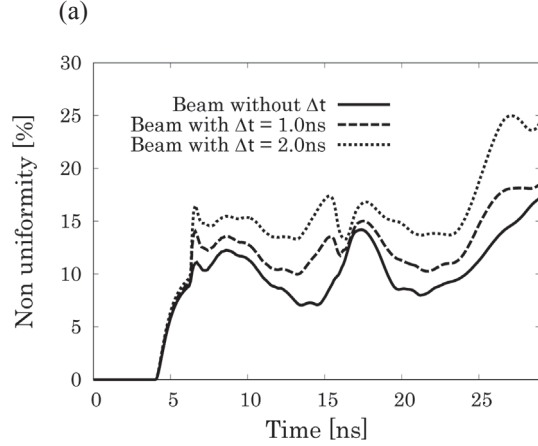


Fig. 6 Non-uniformity histories. One HIB's illumination timing error introduces the overall HIBs illumination non-uniformity. When Δt is positive, one HIB reaches onto a target surface. When Δt is negative, the HIB comes earlier than other HIBs.

uniformity. When Δt is positive, one HIB reaches onto a target surface. When Δt is negative, the HIB comes earlier than other HIBs. In this paper we show just one HIB's illumination timing error effect on the fuel implosion. When Δt is negative and one HIB comes earlier than other HIBs. The initial HIBs illumination non-uniformity must be large. Therefore, Fig. 6(b) shows a relatively large HIBs illumination non-uniformity.

Figure 7 presents a relation between Δt and the fusion energy gain. The results in Fig. 7 show that the HIB timing error allowance would be around ± 1 ns in the HIF target implosion in order to obtain the sufficient fusion energy output.

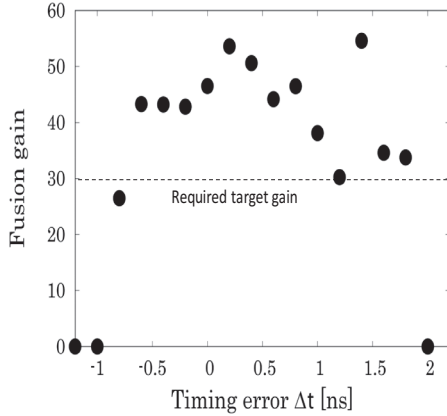


Fig. 7. Fusion energy gain vs. HIB illumination timing error Δt . When Δt is positive, one HIB arrives at the fuel target later. When Δt is negative, the HIB reaches the target earlier than other HIBs. The simulation results suggest that the HIB illumination timing error allowance would be less than 1ns.

In addition, we also check the timing error effect for all the 32 HIBs onto the fuel target gain. In this case, the HIBs timing errors are introduced by using a normal random number. The simulation results show that the allowable Δt would be $-0.1\text{ns} < \Delta t < 0.1\text{ns}$. The results demonstrate that the HIBs illumination timing error has a significant influence to the fuel target implosion performance and should be reduced less than 0.1ns.

4. Conclusions and discussions

In this paper we have presented that the wobbling HIBs mitigate the HIBs illumination nonuniformity successfully, and also that the HIB illumination timing error should be less than 0.1ns.

The wobbling HIBs induces a small implosion acceleration oscillation in time and space, which introduces the HIBs illumination smoothing. In HIF, the higher wobbling frequency more than 150MHz helps to improve the fusion energy output. HIF accelerators would have a capability to apply the wobbling motion of up to 1GHZ or so [11, 12]. In addition, the wobbling beam based non-uniformity mitigation mechanism would be one of the general phase-control non-uniformity mitigation mechanism [2, 5, 6]. The phase control non-uniformity mitigation mechanism would be applicable to other plasma instabilities and non-uniformity smoothing.

Acknowledgements

The work was partly supported by JSPS, MEXT, CORE (Center for Optical Research and Education, Utsunomiya University), and ILE/Osaka University.

References

- [1] S. Atzeni, and J. Meyer-ter-Vehn: The Physics of Inertial Fusion, (Oxford Science Pub 2004).
- [2] S. Kawata, T. Karino, and A.I. Ogoyski: Matter and Radiation at Extremes 1, 89 (2016).
- [3] M. H. Emery, J. H. Orens, J. H. Gardner, and J. P. Boris, Phys. Rev. Lett. 48, 253 (1982).
- [4] S. Kawata, and K. Niu: J. Phys. Soc. Jpn. 53, 3416 (1984).
- [5] S. Kawata, Phys. Plasmas 19, 024503 (2012).
- [6] S. Kawata, and T. Karino: Phys. Plasmas 22, 042106 (2015).
- [7] S. Kawata, Y. J. Gu, X. F. Li, T. Karino, H. Katoh, J. Limpouch, O. Klimo, D. Margarone, Q. Yu, Q. Kong, S. Weber, S. Bulanov and A. Andreev, Phys. Plasmas 25, 011601 (2017).
- [8] S. Kawata, T. Sato, T. Teramoto, E. bandoh, Y. Masubichi, H. Watanabe, and I. Takahashi, Laser Part. Beams 11, 757 (1993).
- [9] S. Kawata, T. Karino, and Y. J. Gu, High Power Laser Science and Engineering 7, e3, (2019).
- [10] S. Skupsky and K. Lee: J. Appl. Phys. 54, 3662 (1983).
- [11] H. Qing, R. C. Davidson, Phys. Rev. Lett. 104, 254801 (2010).
- [12] B. Y. Sharkov, et al., Matter and Radiation at Extremes, 1, 28(2016).

Soft X-Ray Radiation from CO₂, N₂ and C₃H₈ Discharges in the Divergent Gas-Puff Z Pinch

Keiichi Takasugi, Mineyuki Nishio*

Institute of Quantum Science, Nihon University

**Anan College, National Institute of Technology*

ABSTRACT

Study of point radiation source in the “water window” region was conducted by using the divergent gas-puff z pinch. CO₂, N₂ and C₃H₈ were used as the operating gas. Spectra of H-like C and He-like C were observed from the C₃H₈ discharge. Hot spots were observed from each observation by the soft x-ray CCD camera. Imaging of small organisms was attempted using soft x-ray radiated from hot spots.

Keywords

Divergent gas-puff z pinch, Hot spot, Soft x-ray, K-shell radiation, Water window

1. Introduction

Gas-puff z pinch is an efficient soft x-ray radiation source capable of repeated discharge[1]. Plasma focus can also cause plasma to converge to a single point reproducibly. The divergent gas-puff z pinch has been devised for the realization of a highly efficient point radiation source having these advantages[2].

The divergent gas-puff z pinch performs gas puff from the inner electrode, the plasma shrinks three-dimensionally, and a hot spot is generated in front of it. Efficient energy input is possible compared to the conventional gas-puff z pinch[3]. K-shell radiation and L-shell radiation have been observed from Ar pinch plasmas[4, 5, 6].

The wavelength region ranging from 2.3 nm to 4.4 nm is called the “water window”, which makes it possible to stand out organic matter in the water. Conventionally, synchrotron radiation and laser produced plasma have been used as the radiation source. In this study, CO₂, N₂ and C₃H₈ discharges were conducted using the divergent gas-puff z pinch to realize a simple and efficient point radiation source in the “water window” region.

2. Experimental Setup

The experiment was conducted on the SHOT-GUN III z-pinch device at Nihon University(Fig. 1). The energy storage section of the device consists of a capacitor bank of 40 kV 12 μ F with a maximum current of 300 kA. The feature of this device is that it can be charged both positive and negative. In this experiment, the charging was made to a negative voltage to suppress the generation of hard x-ray.

The gas-puff was made by a high-speed gas valve installed in the inner electrode and a divergent annular Laval nozzle provided on the electrode. The divergence angle of the nozzle was 10 degrees with respect to the central axis. The diameter of the nozzle was 30 mm, and the outer electrode has a hole of 60 mm. The distance between the inner electrode and the outer electrode was 30 mm.

Discharge currents were measured by Rogowski coils placed on the input side and the load side. A scintillation probe (SCI) using 3 mm thick plastic scintillator was used to monitor soft x-ray. Because there was a Be window of 15 μ m, the soft x-ray of 1 keV or less attenuated greatly. To monitor soft x-ray and

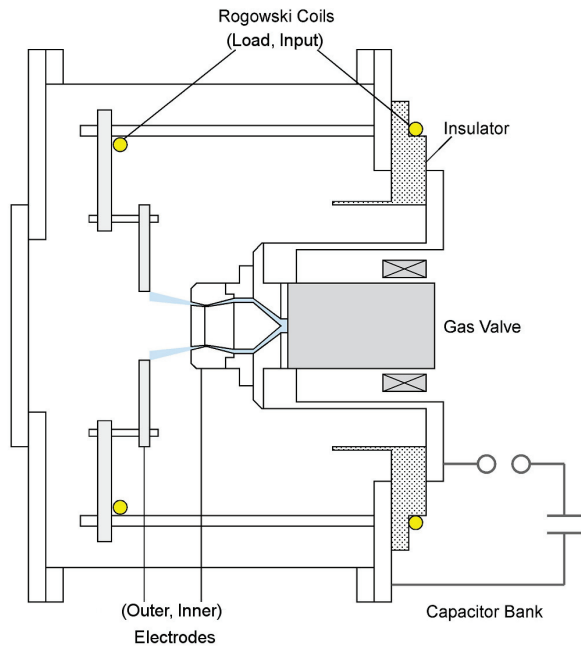


Fig. 1: Schematic diagram of the SHOTGUN III divergent gas-puff z-pinch device. The gas is puffed from the annular Laval nozzle mounted on the inner electrode.

extreme ultraviolet light, an x-ray diode (XRD) with a filterless Ni photocathode was used. Since the XRD was not calibrated, absolute amount could not be measured, but it had a wide sensitivity range from ultraviolet light to soft x-ray[7].

Hot spots were observed using a pinhole camera equipped with a CCD. The CCD made by Laser-Laboratorium Göttingen e.V. was used. The sensitive wavelength region was $< 1 \text{ nm} \sim 1,100 \text{ nm}$, and the pixel size was $6.45 \mu\text{m}$, $1,392 \times 1,040$ pixels. A pinhole of $30 \mu\text{m}$ in diameter and an Al-coated Mylar filter of $4 \mu\text{m}$ in thickness were used. The same CCD was used to take radiographs of small organisms. The images were colored using NIH ImageJ software.

Soft x-ray spectroscopic measurement was performed using a glazing incidence spectrograph equipped with a diffraction grating. The spectrometer was manufactured by Toyota Macs Inc. and could perform 3-20 nm spectrometry[6]. Kodak BioMax MS film was used for spectral recording.

Ion	H-like 1s-2p	He-like 1s ² -1s2p
C	3.373 nm	4.027 nm
N	2.478 nm	2.879 nm
O	1.897 nm	2.160 nm
Ne	1.214 nm	1.345 nm
Ar	0.373 nm	0.395 nm

Table 1: K-shell radiation spectra of H-like and He-like ions.

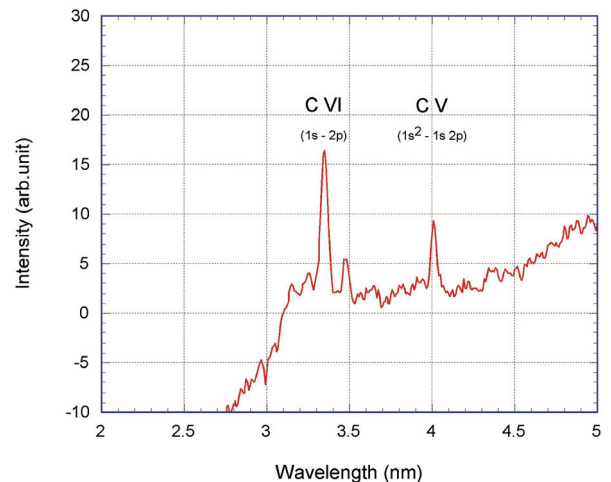


Fig. 2: Soft x-ray spectra of C_3H_8 discharge in the divergent gas-puff z pinch.

3. Soft X-Ray Spectra

Table 1 shows the spectra of K-shell radiation emitted from multiply ionized ions at high temperature. H-like Lyman- α line and He-like resonance line are expected to be emitted easily. Of these, C and N have these spectra in the “water window” region.

Spectra of soft x-ray emitted from hot spots were observed using the glazing incidence spectrograph. C_3H_8 gas was used, the filling pressure was 2 atm and the charging voltage was -25 kV. Figure 2 shows the spectra. Lyman- α line (3.373 nm) of H-like C ion and resonance line of He-like C ion (4.027 nm) were observed. No other radiation was observed. No spectroscopic measurements were made on the N_2 and CO_2 discharges, but it was expected that there would be radiation of N ions and O ions as well.

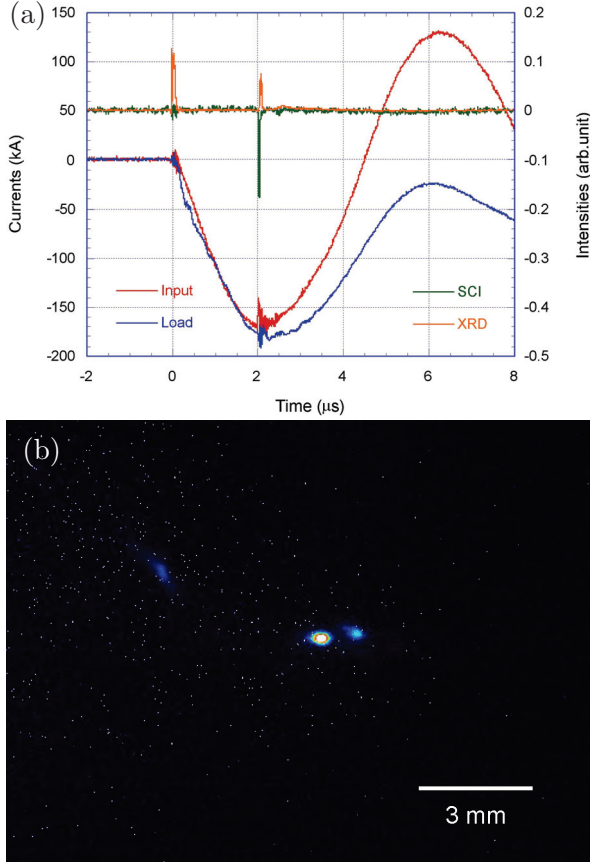


Fig. 3: (a) Discharge currents and x-ray signals and (b) CCD image of CO₂ discharge in the divergent gas-puff z pinch.

4. Hot Spot Formation

First CO₂ discharge was conducted. The plenum pressure was 5 atm and the charging voltage was -25 kV. Figure 3(a) shows the current waveforms and x-ray signals of the CO₂ discharge. Pinch occurred at time 2.03 μ s, and a dent occurred in the current waveform. The input current just before the pinch was -178 kA. There is a difference between the input current and the load current after pinching because of a short circuit behind the internal electrode. Spiked SCI signal and XRD signal were observed along with pinch. The pulse width of SCI was 20 ns and the pulse width of XRD was 64 ns. Figure 3(b) shows a soft x-ray image of the CO₂ discharge. The inner electrode was on the right side, the direction of the discharge axis was the horizontal direction and the radial direction was the vertical direction. A hot spot was

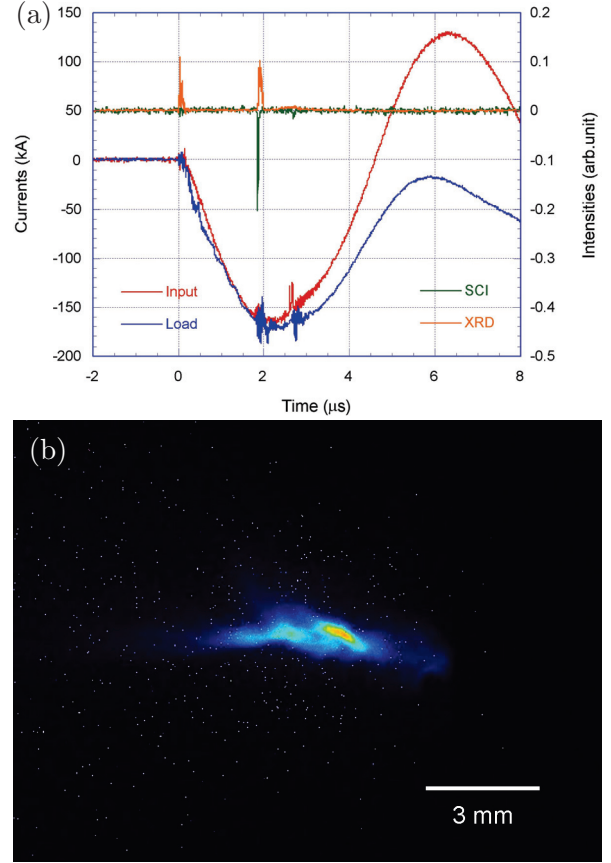


Fig. 4: (a) Discharge currents and x-ray signals and (b) CCD image of N₂ discharge in the divergent gas-puff z pinch.

observed in front of the inner electrode. The diameter of the hot spot was about 300 μ m, and the length was about 400 μ m.

Next, N₂ discharge was conducted. The plenum pressure was 5 atm and the charging voltage was -25 kV. Figure 4(a) shows the current waveforms and x-ray signals of the N₂ discharge. Pinch occurred at time 1.81 μ s, and a dent occurred in the current waveform. The input current just before the pinch was -159 kA. Spiked SCI signal and XRD signal were observed along with pinch. The pulse width of SCI was 16 ns and the pulse width of XRD was 76 ns. Figure 4(b) shows a soft x-ray image of the N₂ discharge. Periodic structure appeared and it was thought that a helical instability occurred. The diameter of the hot spot was about 300 μ m, and the length was about 1,000 μ m.

Next, C₃H₈ discharge was conducted. The plenum pressure was 2 atm and the charging

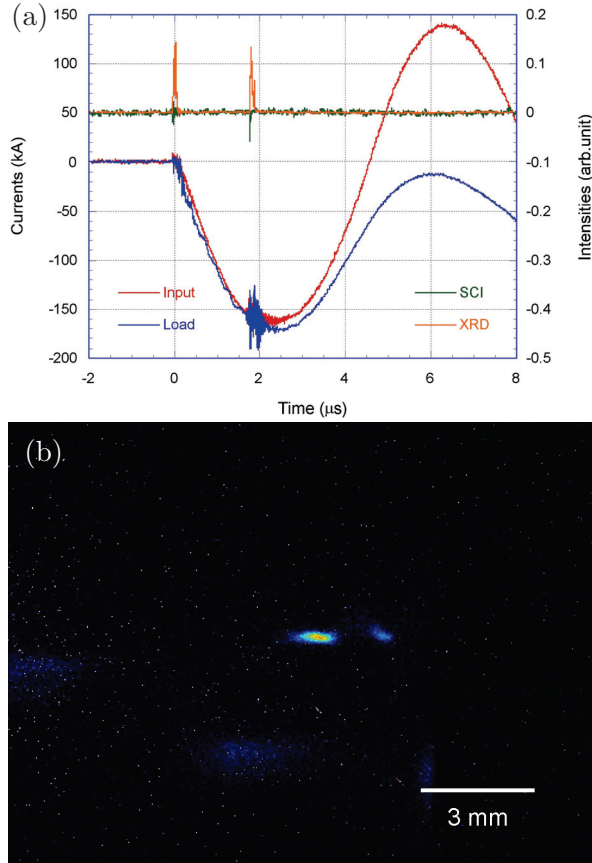


Fig. 5: (a) Discharge currents and x-ray signals and (b) CCD image of C_3H_8 discharge in the divergent gas-puff z pinch.

voltage was -25 kV. Figure 5(a) shows the current waveforms and x-ray signals of the C_3H_8 discharge. Pinch occurred at time 1.76 μs , and a dent occurred in the current waveform. The input current just before the pinch was -154 kA. Spiked SCI signal and XRD signal were observed along with pinch. The pulse width of SCI was 12 ns and the pulse width of XRD was 48 ns. The SCI signal was weak. It was considered that this was due to the strong attenuation by the filter. Figure 5(b) shows a soft x-ray image of the C_3H_8 discharge. The diameter of the hot spot was about 200 μm , and the length was about 700 μm . All the radiation levels were sufficient to observe with CCD through the pinhole.

5. Soft X-Ray Radiography

Imaging of small organisms was carried out using soft x-ray emitted by discharges using three kinds of gases. Daphnias were used for the sample and placed in the vacuum chamber. In order to block visible light and hold the sample, Be of thickness 15 μm and Kapton of thickness 7.5 μm were used.

Figure 6 shows soft x-ray radiographs of daphnias projected onto the CCD. (a) shows CO_2 discharge, (b) shows N_2 discharge, and (c) shows C_3H_8 discharge. The daphnias were taken with clear illuminance at the CO_2 discharge. With the N_2 discharge, the illuminance was somewhat lower, but the structure of daphnia was able to be recognized. At the C_3H_8 discharge the illuminance was very low and it was dark. Since the emission spectrum differed depending on the gas, the absorption by the filter was greatly different and it was considered that the illuminance greatly differed.

6. Summary

Study of point radiation source in the “water window” region was conducted by using the divergent gas-puff z pinch. The states of pinch discharges were examined for CO_2 , N_2 and C_3H_8 .

Lyman- α line of H-like C ion and resonance line of He-like C ion were observed from the C_3H_8 discharge. These spectra are the radiation sources in the “water window” region.

Discharges were observed by the soft x-ray CCD camera. Spot-like radiation sources were observed for CO_2 , N_2 and C_3H_8 respectively. In the N_2 discharge, a periodic structure, which appeared to be a helical instability, was observed.

Imaging of daphnias were attempted using soft x-ray radiated from hot spots. With the CO_2 and N_2 discharges it was possible to observe the structure of daphnia with an appropriate illuminance. Since the emission spectrum differs depending on the gas, the absorption by the filter greatly affected. It is thought that the radiation can be used for tissue observation in the “water window” region by using an appropriate filter.

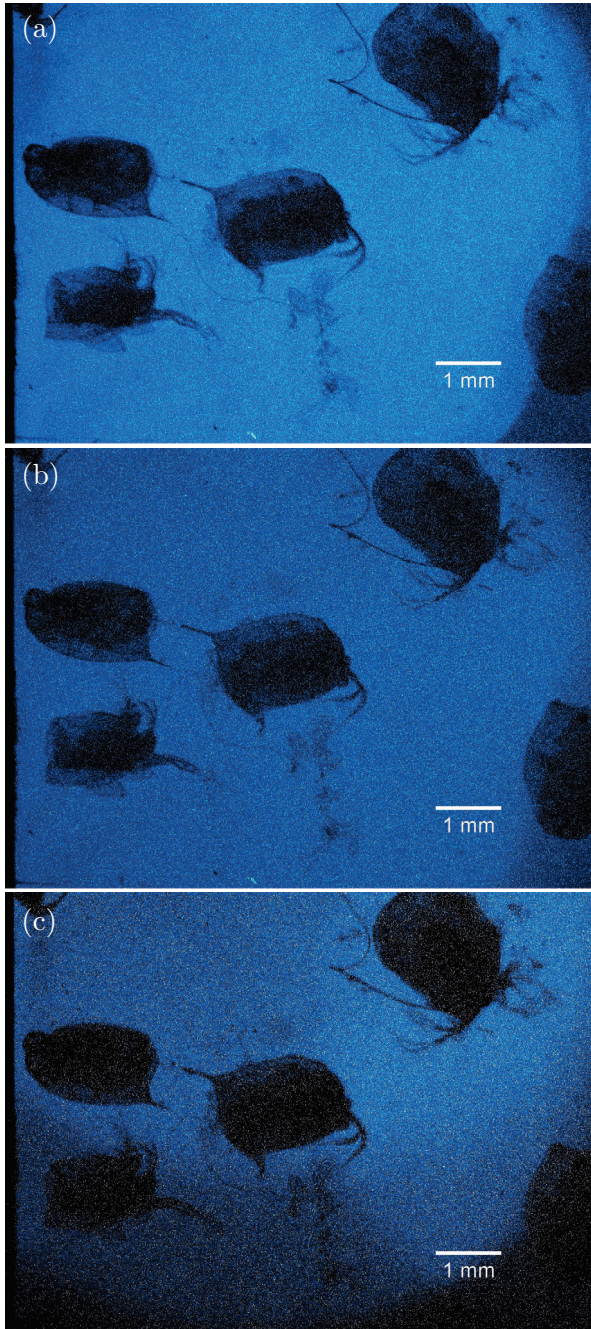


Fig. 6: Soft x-ray radiographs of daphnias taken by (a) CO_2 , (b) N_2 and (c) C_3H_8 discharges in the divergent gas-puff z pinch.

References

- [1] J. Shiloh, A. Fisher and N. Rostoker: *Phys. Rev. Lett.* **40**, 515 (1978).
- [2] K. Takasugi and E. Kiuchi: *Plasma Fusion Res.* **2**, 036 (2007).
- [3] K. Takasugi and E. Kiuchi: *NIFS-PROC* **72**, 17 (2008).
- [4] E.O. Baronova, K. Takasugi, V.V. Vikhrev and T. Miyamoto: *Proc. 13th Int. Conf. Particle Beams*, 784 (2001).
- [5] K. Takasugi and H. Akiyama: *Jpn. J. Appl. Phys* **43**, 6376 (2004).
- [6] F. Kobayashi and K. Takasugi: *NIFS-PROC* **62**, 10 (2006).
- [7] R. H. Day, P. Lee, E. B. Saloman, and D. J. Nagel: LA-7941-MS (1981).

Spectroscopic measurement of active species generated in streamer discharge on water surface

Takuya Hayashi, Souhei Toyoda, Tomokazu Kanna, Takashi Sakugawa

Kumamoto University

ABSTRACT

Studies on active species generation characteristics such as OH radicals in streamer plasma progressing by discharge have not been conducted sufficiently. From this background, we analyze the light emitted by the plasma on the water surface and investigate the generation characteristics of the active species in the streamer plasma. Therefore, in this study, we investigated the relationship between the position of pulsed discharge plasma on the water surface and the OH radical generation characteristics when pulse 1 shot was applied.

Keywords

Pulsed power, Streamer discharge, OH radical

1. Introduction

Pulse power is electromagnetic energy compressed temporally or spatially, and it is possible to realize a high energy state with less energy. Given this pulse power on the water surface, it is possible to cause a streamer discharge on the water surface [1].

Since the discharge on the water surface deals with gas, liquid, plasma and complicated regions, the generation characteristics of OH radicals are not yet elucidated. In the future, in order to advance the application, it is required to elucidate the control method of the discharge on the water surface suitable for OH radical generation [2].

In this study, we investigate the influence of the position of the ground electrode on OH radical

generation in streamer discharge on water surface.

Normally, the streamer discharge progresses radially as shown in Fig. 1, but by using the guide, it is possible to summarize the progress direction as shown in Fig. 2

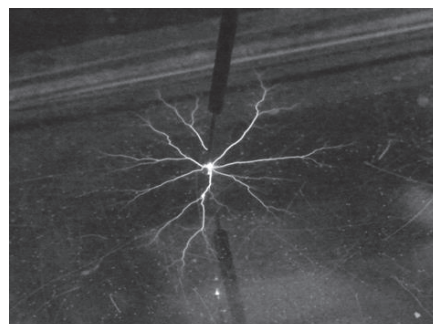


Fig.1. Streamer discharge



Fig.2. Streamer discharge controlled in direction of development

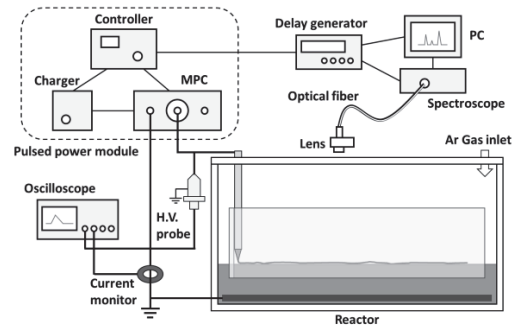
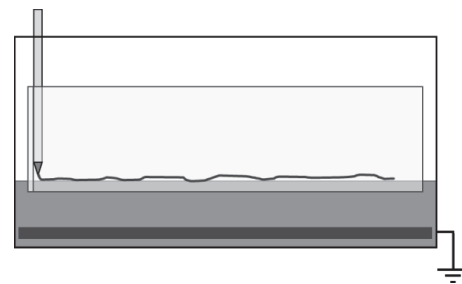


Fig.3. Experimental device

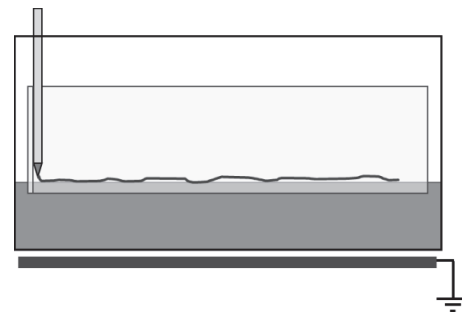
2. Experimental Setup

Fig.3 shows experimental device. 0.5 JMPC is used for power supply. For normal spectroscopy, a trigger signal is sent from the MPC controller to the spectroscope. The condenser lens is installed in the lid part of the reactor vessel, and light is taken into the spectroscope through a fiber probe. As the power supply setting, the applied energy is set to 45 mJ. The reactor vessel made of acrylic, whose dimensions are 10 by 20 by 10 cm is sealed with argon to make streamer longer. Also, the amount of water in the vessel is 500 mL, and the conductivity is adjusted to 100 uS/cm close to the value of tap water. The electrode used is like this, the high voltage electrode is placed at a position a few mm above the water surface. And the ground electrode is placed at the bottom inside the vessel or under the vessel like fig.4.

Fig.5 shows the spectroscopic position. The position where spectroscopy is performed is set to be 5 cm, 7.5 cm, 10 cm, 12.5 cm away horizontally from the needle electrode.

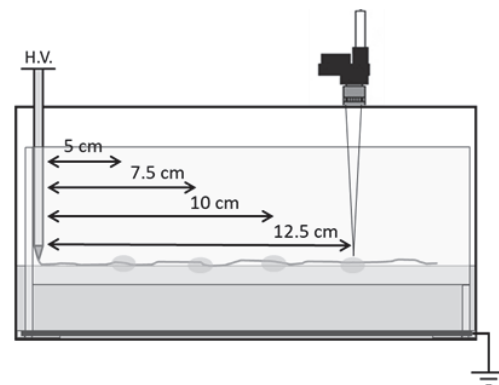


(a) Inner Ground electrode

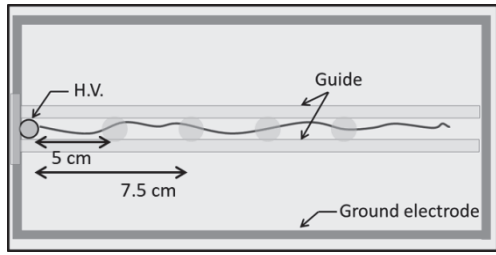


(b) Outer Ground electrode

Fig.4. Reactor diagram



(a) Side view

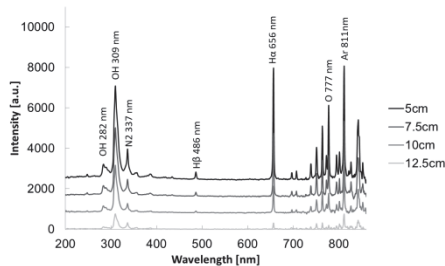


(b) Over view

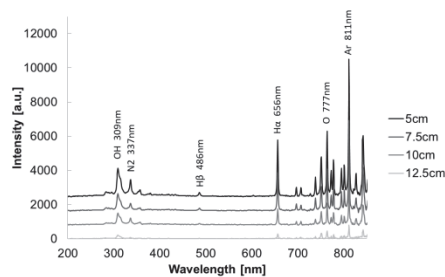
Fig.5. Spectroscopic position

3. Results and Discussion

Fig.6 shows the spectroscopic result. This graph shows a relation of wavelength and intensity of active species. At 309 nm, OH radical is observed. At 656 nm, H α is observed. At 777 nm, O is observed. In the range of 700 nm to 850 nm, light due to argon which is an atmospheric gas was observed. And the emission intensity decreases as the distance from the needle electrode increases.



(a) Inner Ground

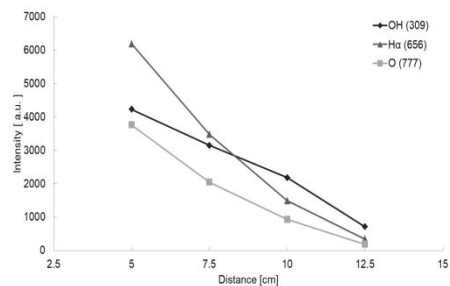


(b) Outer Ground

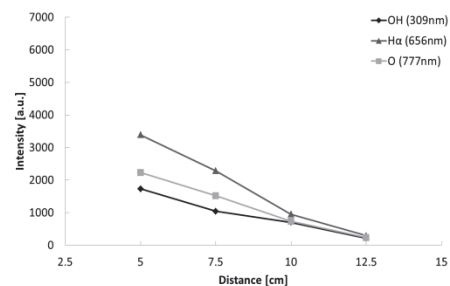
Fig.6. Emission spectrum

Fig.7 shows the relationship between the

distance of the OH radical, H α and O from the needle electrode and the emission intensity. When the ground electrode is placed inside the container, At 5, 7.5 cm position, the emission intensity of H α is the largest among three. And at 10, 12.5 mm position, the emission intensity of OH radical is the largest. This is thought to be due to the fact that the electric field concentrates and the energy given to water increases at the position of 5, 7.5 cm close to the electrode. OH radical as molecules are decomposed and hydrogen atoms and oxygen atoms are generated. When the ground electrode is placed outside the vessel, the emission intensity of OH is smallest regardless of the distance from the high voltage electrode.



(a) Inner Ground

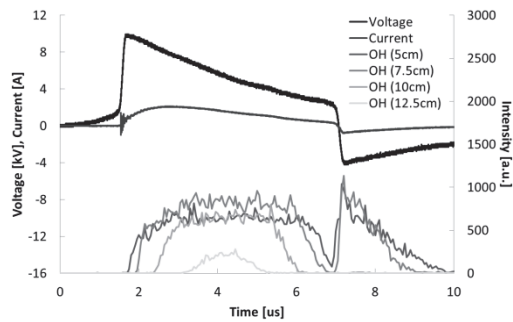


(b) Outer Ground

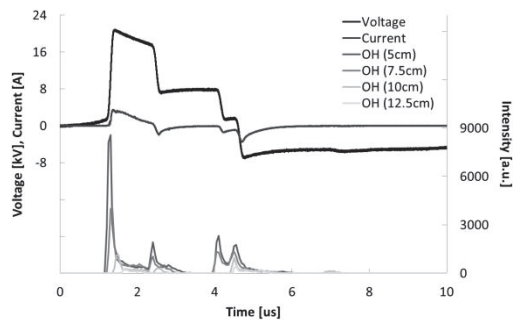
Fig.7. Position characteristics of emission intensity

Fig.8 (a) shows time resolved spectroscopic

result when the ground electrode is placed inside the container. The emission per unit time of OH radical is approximately saturated. Fig.8 (b) shows result when the ground electrode is placed outside the container. The emission by OH is the largest when the first voltage and current rise. After that, the emission of OH sharply decreases.



(a) Inner Ground



(b) Outer Ground

Fig.8. Time resolved spectroscopy result

4. Conclusions

In this research, the influence of the positional configuration of the ground electrode on the emission characteristics of OH radicals was investigated. When the ground electrode is placed outside the vessel, OH radicals emit strongly when the voltage rises. Further, the integrated value is about 0.3 to 0.4 times as compared with the case where the ground electrode is disposed inside.

References

- [1] S. Kanazawa, H. Kawano, S. Watanabe, T. Furuki, S. Akamine, R. Ichiki, T. Ohkubo, M. Kocik and J. Mizeraczyk, "Observation of OH radicals produced by pulsed discharge on the surface of a liquid", Plasma Sources Sci. Technol., 20 (2011) 034010
- [2] H Akiyama, "Streamer discharges in liquids and their applications", IEEE Transactions on Dielectrics and Electrical Insulation, Vol.7, issue.5, pp.646-653, (2000)

Comparison of stopping range and blister skin thickness generated by 4 MeV helium ion beam in tungsten

Yuki Uchida, Seiki Saito*, Nobuo Saito, Tsuneo Suzuki,
Kazumasa Takahashi, Toru Sasaki, Takashi Kikuchi

Nagaoka University of Technology

**Yamagata University*

ABSTRACT

4 MeV helium ion beams were irradiated with a tungsten sample in order to assess the irradiation effect on first wall materials in magnetic confinement nuclear fusion systems. Blisters were obtained on a surface of the irradiated sample. The blister skin thickness was greater than the stopping range of 4 MeV helium ion in tungsten. The result may be a problem to design the thickness of first wall in future nuclear fusion reactors.

Keywords

Magnetic confinement fusion, First wall, Helium ion, Tungsten, Blister, High-energy ion beam

1. Introduction

Helium ions at energy of 3.5 MeV are emitted by deuterium-tritium (DT) reaction in magnetic confinement nuclear fusion systems. They shared their kinetic energy to a fuel plasma and are irradiated to plasma-facing components with wide energy ranges. Thus, plasma-facing materials are exposed to particle loading. Tungsten is a candidate of plasma-facing materials, because it has convenient properties such as low sputtering yield and high melting point [1].

Low-energy helium ions (<keV) are irradiated to divertor plates along with magnetic flux lines. Helium bubble [2] and filament structure [3,4] were observed on a surface of tungsten.

It is predicted that high-energy helium ions (~MeV) can be irradiated to the first wall due to toroidal magnetic field ripple loss, plasma disruption or magnetohydrodynamic instability as an edge localized mode (ELM). Especially, the effect of the ripple loss was calculated numerically with a sharp peak of kinetic energy at 3.5 MeV and particle flux of $10^{18} \text{ m}^{-2}\text{s}^{-1}$ [5]. Formation of blisters on tungsten samples was reported implanting with 1.3 MeV helium beams at 1123 K [6]. On the other hand,

helium bubble and void are produced in temperature regimes in $0.2\text{--}0.4 T_m$, where T_m is the melting point of tungsten [7]. In addition, vacancy inside tungsten is movable in 473 K [8]. Therefore, helium bubbles or blisters may be generated in the low-temperature condition below 1000 K.

This paper reports the feature of blisters produced by high-energy helium ion beams of the low-temperature condition. Especially, the blister skin thickness is observed and compared with stopping range of helium ion in tungsten.

2. Experiment

An electrostatic tandem accelerator at Nagaoka University of Technology was used to irradiate the helium ion with a tungsten sample. Kinetic energy of helium ion was set to 4 MeV in order to demonstrate the helium ion generated by DT reaction. A polycrystalline tungsten thin plate (Nilaco corporation) was adopted as a sample. It was fabricated by powder metallurgy in purity of 99.95%. Table 1 shows the experimental condition for irradiation of helium ion in tungsten.

Table 1 Experimental condition for irradiation of helium ion to tungsten.

Target	Tungsten (W)
Beam Ion	Helium (He^{2+})
Kinetic energy	4 MeV
Ion flux	$10^{18} \text{ m}^{-2}\text{s}^{-1}$
Ion fluence	10^{22} m^{-2}
Surface temperature	288–332 K

More detailed description of the experimental arrangement has been reported in Refs. [9,10].

After irradiation experiment, three independent blisters were observed on the surface of the tungsten sample. The cross-section of each blisters was formed on the tungsten surface with a focused ion beam (FIB) instrument. The cross-section of each blister was observed with a scanning electron microscopy (SEM), and the blister skin thickness, i.e. a spherical shell of blister or distance between the surface of tungsten and crack position, was measured.

Figure 1 shows (a) cross-sectional view and (b) side view of blister skin. Figure 1 (a) corresponds to a secondary electron image observed by SEM. Thus, the length p can be measured by SEM. p is a projection of net blister skin thickness t as described in Fig. 1 (b). Therefore, t is calculated by

$$t = p / \sin \theta. \quad (1)$$

Here, θ denotes the tilted angle to observe the cross-section. In this case, θ was set to 60° .

3. Results and Discussion

Three blisters named blister (a), (b) and (c) were observed on the irradiated sample. Table 2 shows the blister skin thickness t and stopping ranges calculated by various programs. Amounts of t were evaluated as minimum and maximum values. The stopping ranges of 4 MeV helium ion in tungsten were calculated by three programs: SRIM [11], ASTAR [12] and ATIMA [13]. All of blister skin thicknesses were greater than all of stopping ranges.

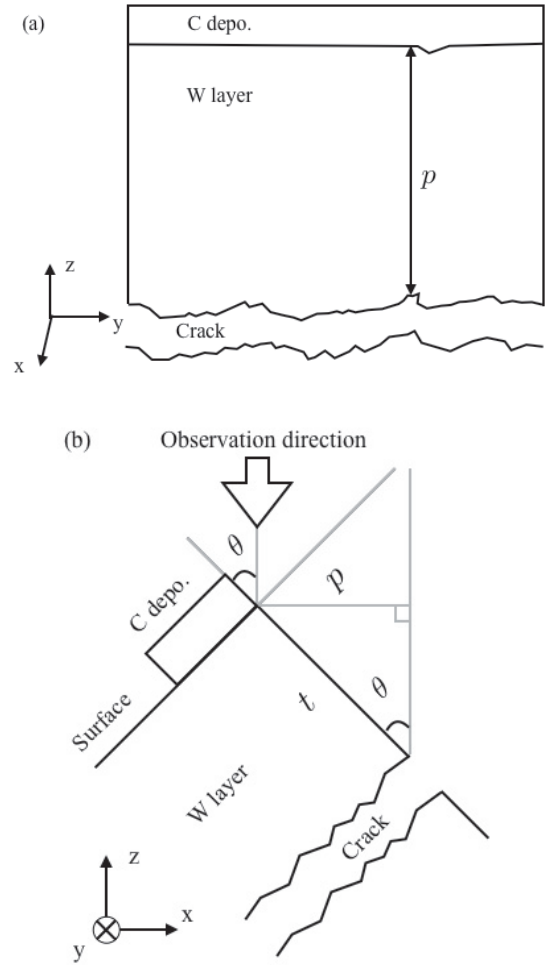


Fig. 1 (a) cross-sectional view and (b) side view of blister skin

Table 2 Blister skin thickness t and stopping ranges calculated by various programs.

Blister	(a)	(b)	(c)
$t, \mu\text{m}^*$	8.5–8.9	7.4–8.1	6.8–7.3
SRIM[11], μm		6.02	
ASTAR[12], μm		6.12	
ATIMA[13], μm		6.64	

*Minimum and maximum values were shown.

A mechanism of blister formation is suggested as a gas pressure model [14] that gas bubbles were interconnected in the material, and plastic deformation occurs due to the gas pressure to form the blister. According to this model, the size of gas bubbles should be increased in the material to form a blister. Moreover, the position at which gas bubbles

exist must be around the stopping range of helium in tungsten. However, the experimental results in this study were different from the stopping range on the order of μm .

Fenske et al. compared with blister skin thickness and stopping range of helium in niobium with 20 keV and 500 keV of helium ion beam [15]. The thickness is greater than the stopping range when the kinetic energy of the helium ion is 20 keV. This result corresponds to our result. However, at 500 keV, the thickness is nearly equal to the stopping range. This result is different from our result. Thus, it is considered that the relationship of blister skin thickness and stopping range is changed by the kinetic energy of ion. Describing the reason why the skin thickness differs from the stopping range, we considered that implanted helium is moved in tungsten. In addition, these are concentrated at a position deeper than the stopping range.

If a blister is grown, exfoliation occurs. This phenomenon decreases the wall thickness in fusion systems. Degrees of the decreasing wall thickness could depend on blister skin thickness. Thus, the fact that blister skin thickness is greater than the stopping range is difficult to design the wall thickness in a future fusion reactor.

4. Conclusions

In this study, the effect of helium irradiation in tungsten was investigated in sight of blister formation. Helium ion beams were irradiated to the polycrystalline tungsten plate in the condition of 4 MeV, 10^{22} ions/ m^2 and 332 K. The three blisters were observed on the surface of the irradiated sample. Measured blister skin thicknesses in the range of 6.8–8.9 μm were greater than the calculated stopping range in the range of 6.02–6.64 μm . This trend corresponds to the other result irradiated by 200 keV helium ions in niobium from Fenske [15], although it differs from another result of 500 keV [15]. The result may be a problem to design the thickness of the first wall in a future nuclear fusion reactor.

References

- [1] A.R. RAFFRAY et al., “Dynamic chamber armor behavior in IFE and MFE”, *Fusion Engineering and Design*, **63–64**, pp.597–608 (2002).
- [2] M. YAMAGIWA et al., “Helium bubble formation on tungsten in dependence of fabrication method”, *Journal of Nuclear Materials*, **417**, pp.499–503 (2011).
- [3] S. SAITO et al., “Determination of dynamical changes in sputtering and retention on bubble-growing tungsten under helium plasma irradiation by binary-collision-approximation-based simulation”, *Japanese Journal of Applied Physics*, **55**, pp.01AH07-1–01AH07-7 (2016).
- [4] S. KAJITA et al., “Development of Nanostructured Black Metal by Self-Growing Helium Bubbles for Optical Application”, *Japanese Journal of Applied Physics*, **50**, pp.08JG01-1–08JG01-4 (2011).
- [5] K. TOBITA et al., “First wall issues related with energetic particle deposition in a tokamak fusion power reactor”, *Fusion Engineering and Design*, **65**, pp.561–568 (2003).
- [6] S.B. GILLIAM et al., “Retention and surface blistering of helium irradiated tungsten as a first wall material”, *Journal of Nuclear Materials*, **347**, pp.289–297 (2005).
- [7] R.W. HARRISON et al., “Engineering self-organising helium bubble lattices in tungsten”, *Scientific Reports*, **7**, pp.7724-1–7724-8 (2017).
- [8] P.E. LHUILLIER et al., “Positron annihilation studies on the nature and thermal behaviour of irradiation induced defects in tungsten”, *Physica Status Solidi C*, **6**, pp.2329–2332 (2009).
- [9] Y. UCHIDA et al., “Experiment and measurement with high-energy helium irradiation to tungsten using tandem accelerator for divertor in magnetic confinement fusion system”, *Energy Procedia*, **131**, pp.359–362 (2017).
- [10] Y. UCHIDA et al., “Blister Formation on Tungsten Irradiated by 4 MeV Helium Ion Beam

- in Ordinary Temperature”, *Plasma and Fusion Research: Rapid Communications*, **13**, pp.1205084-1–1205084-3 (2018).
- [11] J.F. ZIEGLER et al., “SRIM – The stopping and range of ions in matter (2010)”, *Nuclear Instruments and Methods in Physics Research B*, **268**, pp.1818–1823 (2010).
- [12] ASTAR: <https://physics.nist.gov/PhysRefData/Star/Text/ASTAR.html>
- [13] ATIMA: <https://web-docs.gsi.de/~weick/atima/atima14.html>
- [14] S.K. DAS et al., “Radiation blistering of polycrystalline niobium by helium-ion implantation”, *Journal of Applied Physics*, **44**, pp.25–31 (1973).
- [15] G. FENSKE et al., “Depth Distribution of Bubbles in $^4\text{He}^+$ -Ion Irradiated Nickel and The Mechanism of Blister Formation”, *Journal of Nuclear Materials*, **76&77**, pp.247–248 (1978).

Effect of Electrode Polarity to Atmospheric Pressure Plasma Jet and its Applicability to Surface Modification of Bio-compatible Material

W.T. Leon S. Fernando¹, Ryo Kobayashi¹, Kazumasa Takahashi¹, Takashi Kikuchi¹, Kiyoshi Ohnuma¹, and Toru Sasaki¹

¹ *Nagaoka University of Technology, 1603-1, Kamitomioka, Nagaoka, Niigata 940-2188, Japan*

ABSTRACT

This study focused on developing an alternative approach to address the limitations of conventional low-pressure plasma treatment on bio-compatible materials with a mask. Atmospheric pressure plasma jets provide similar radical generations which require for modifying the surfaces of bio-compatible materials such as polydimethylsiloxane in developing induced pluripotent stem cells at laboratory conditions. A double electrode configured atmospheric pressure plasma jets tend to generate longer plasma jets and with the addition of extra electrode provides a further increase in jet length. Polarity changes in the electrode tend to generate different sizes of atmospheric pressure plasma jets while maintaining similar radical generation such as OH, N, and O. Wetting areas on polydimethylsiloxane surfaces increase with the increase of the irradiation time. Modified polydimethylsiloxane surfaces of irradiation time of 120 s or above show adhere of calcine induced human induced pluripotent stem cells and patterning.

Keywords

Atmospheric pressure plasma jet, polydimethylsiloxane, induced pluripotent stem cells, adhesion, and patterning

1. Introduction

Induced pluripotent stem cells (iPSCs), exhibit infinite self-renewal capacity and differentiation into many cell types [1] [2]. With the introduction of a few specific genes into already specialized somatic cells can be used in a wide range of bio-medicinal application. Applicability of iPSCs widely used in the areas such as, development of regenerative medicines, modeling and investigation of human diseases, drug screening, gene-editing technology, and so on [3].

Development of iPSCs in laboratory conditions requires specific conditions. These conditions can be provided through the cell culture devices which contains properties such as microenvironment of cells, cell-cell interactions, cell-substrate interaction, spatiotemporal distribution of soluble factors, and so on [4] [5]. Polydimethylsiloxane (PDMS) is one of

the most popular bio-compatible material which provides the specific environment for developing iPSCs and it contains properties such as non-toxic, chemically inert, transparent and gas permeable [6].

However, PDMS surfaces were not aided to the cell-substrate interaction and require a surface modification through plasma treatment [7] [8] [9] [10]. For this reason, the low-pressure plasma devices with a mask were used to fabricate the PDMS surfaces [8] [9] [10]. However due to the mask charging and plasma sheath this treatment method limited the wetting sizes on PDMS surfaces to few micrometers [9] [10].

Therefore, our study focused to develop an alternative approach to overcome the limitations created from the low-pressure plasma treatment.

Atmospheric pressure plasma jet (APPJ) was considered for this alteration as it provides a cone shape plasma jet in Z-direction while circular in the X-Y plane. In the present work, considering different properties and setups, APPJs were observed to achieve the possibility of modifying the bio-compatible surfaces. Most suitable APPJ setup further experimented with the surface modification, radical identification through the optical emission spectroscopy (OES), and adhering the human induced pluripotent stem cells (hiPSCs) to the modified surfaces.

2. Experimental Condition and Analyzing Procedures

2.1 Conditions to generate APPJs

Helium (He) gas was used in this study to generate the plasma as it has a low breakdown voltage and providing homogenous uniform plasma. House-made high-voltage and the high-frequency power source was used with the hollow quartz capillary tubes in generating the APPJ. The voltage applied to generate the APPJ was kept almost 18 ± 0.5 kV_{p-p} unless to analyze the voltage effect to the APPJ. Applied voltage and current waveforms are shown in figure 1.

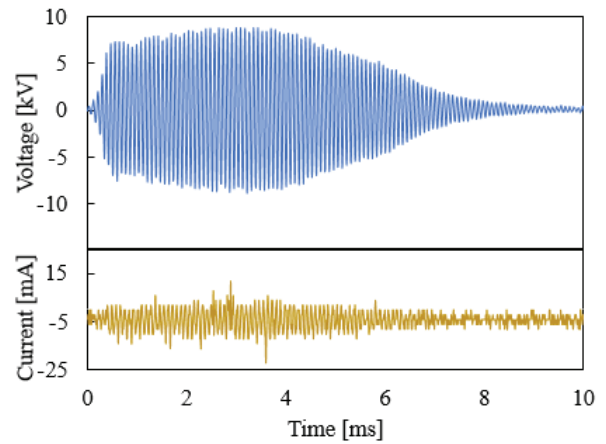


Fig. 1: Applied voltage and current waveforms to generating APPJ

2.2 Determination of length and diameter of APPJ

For this procedure, at first, the generated APPJs were photographed using a digital camera (Fig.2(a)). Next, the images were converted into grey images (Fig.2(b)). Finally, the jet length and the diameter were analyzed using the grey image (Fig.2 (c)).

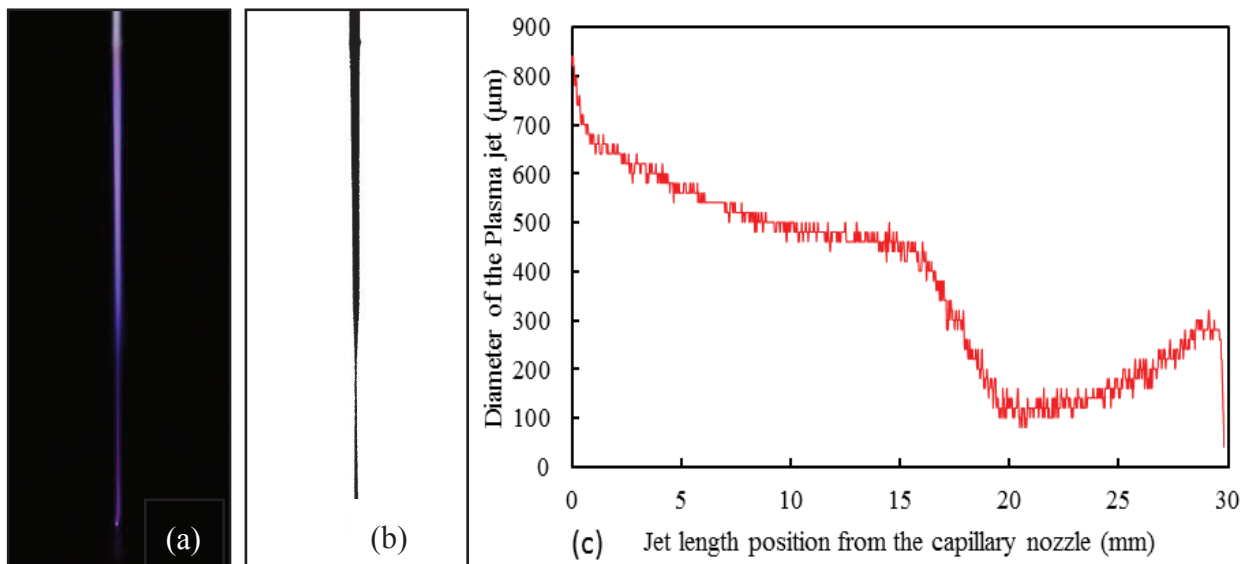


Fig. 2: Procedure in determining APPJ length and its diameter; (a) camera image of the APPJ, (b) grey image of APPJ converted from (a), and (c) jet length and diameter obtained from (b).

2.3 Determination of wetting area (RhodamineB test)

To estimate the wetting areas on APPJ irradiated PDMS surfaces, a chemical procedure was applied. In this procedure a dye known as RhodamineB was used to stain the irradiated PDMS surfaces after 30 minutes of irradiation. Those stained PDMS samples were washed with miliQ water, and washed PDMS samples were observed through the fluorescence spectrometer as shown in figure 3. RhodamineB is adhering to the irradiated surface / modified surface and non-adhere to the non-irradiated surface. This will cause to emit color contrast as shown in figure 3, which were analyzed through ImageJ software for the area estimation [11].

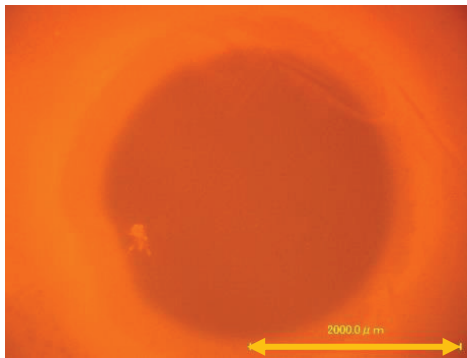


Fig. 3: Fluorescence image of the RhodamineB stained irradiated PDMS surface

3. Results and Discussion

3.1 Comparison between Parallel Electrode and Double Electrode configuration

To determine the optimal APPJ setup for this alternation, two electrode configurations were compared. Capillary tubes with inner diameter of 2.0 mm were used with applying voltage waveform as shown in figure 1. Figure 4 shows the schematics of the parallel electrode (PE) (Fig. 4(a)) and double electrode (DE) (Fig. 4(b)) configurations which were experimented in this study.

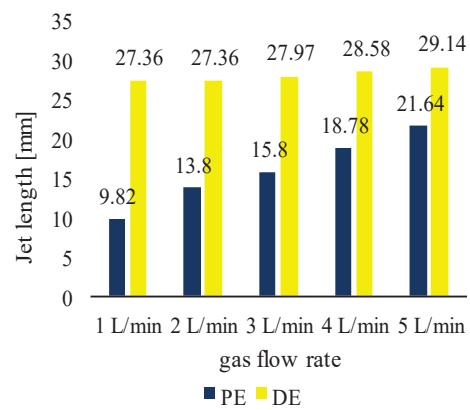


Fig. 5: APPJ length for the PE and DE configurations

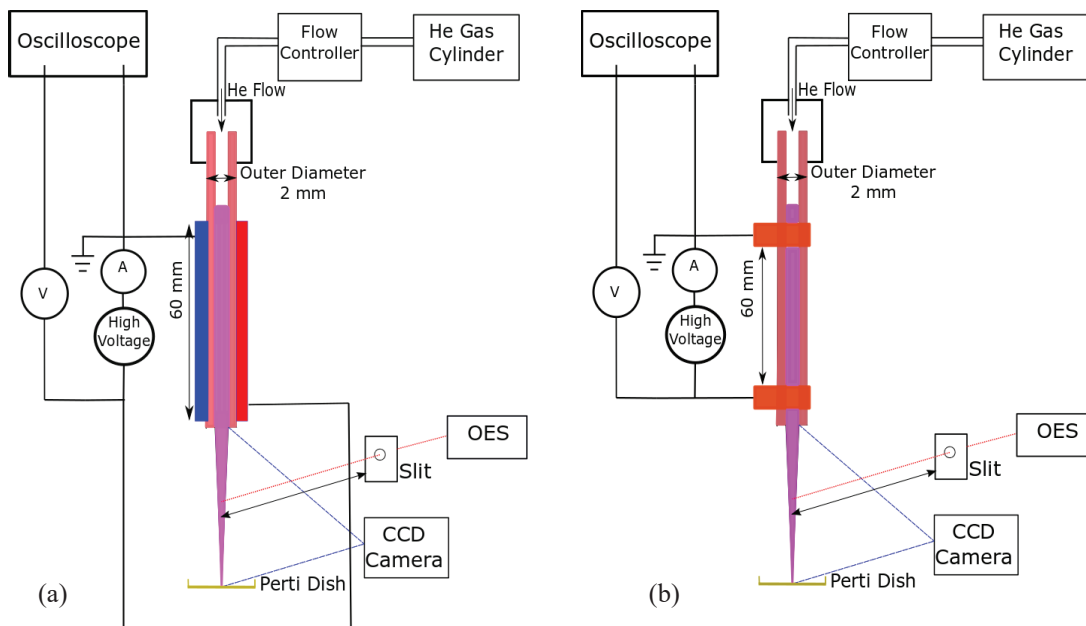


Figure 4: Schematics of the experimental setups; (a) Parallel electrode configuration and (b) Double electrode configuration

Generated APPJs for both the setups were analyzed using the in-house program and compared as shown in figure 5. From the compared results, DE configuration provided longer APPJ comparing to the PE configuration for all the gas flow measurements. For the smooth surface modification of bio-compatible materials, it is necessary to avoid the corona discharges. Hence longer APPJs were suitable to achieve this objective and further modification was done to DE configuration to optimize its plasma jet.

3.2 Addition of extra electrode to the DE configuration

To minimize the reflection effect and generate stable and low radius plasma jet, this study includes an additional electrode to the bottom of the plasma jet for the DE configuration as shown in figure 6 [11]. Tungsten (W) wire with a diameter of 50 μm was used as an additional electrode to achieve this objective and to minimize the localization point of the bottom of the plasma jet as shown in figure 7.

Due to the additional electrode, APPJ was observed to be increased. Figure 8 shows the compared jet length of the APPJ for with and without additional electrode scenarios. This implication state that addition of extra electrode to the bottom of the APPJ can optimize the plasma jet.

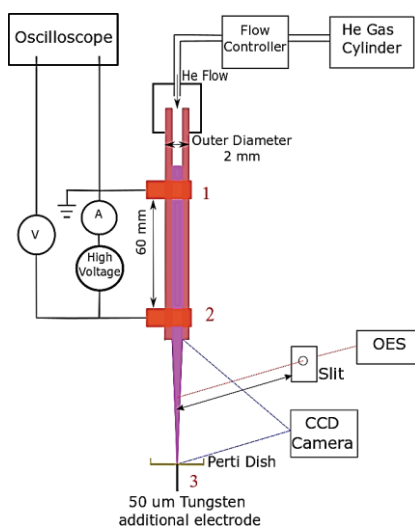


Fig. 6: Schematic of the DE configuration with additional electrode

As the additional electrode increase the jet length, different combinations of polarities were tested to observe the behavior of the APPJ. Table 1 shows the tested polarity combinations and behavior of observed APPJs.



Fig. 7: Digital image of the APPJ with an additional electrode

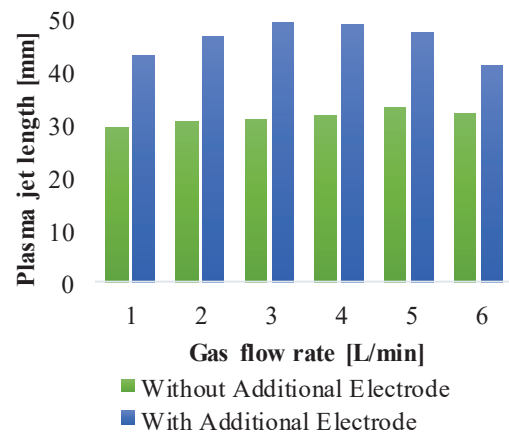


Fig. 8: Comparison graph for the APPJ with and without additional electrode

From these observations, setups A and C provide a suitable APPJ for surface modification. Hence through the OES (Hamamatsu, PMA-12) two APPJs were investigated. Figure 9 shows the OES of both the APPJs in the wavelength range of 200 – 800 nm.

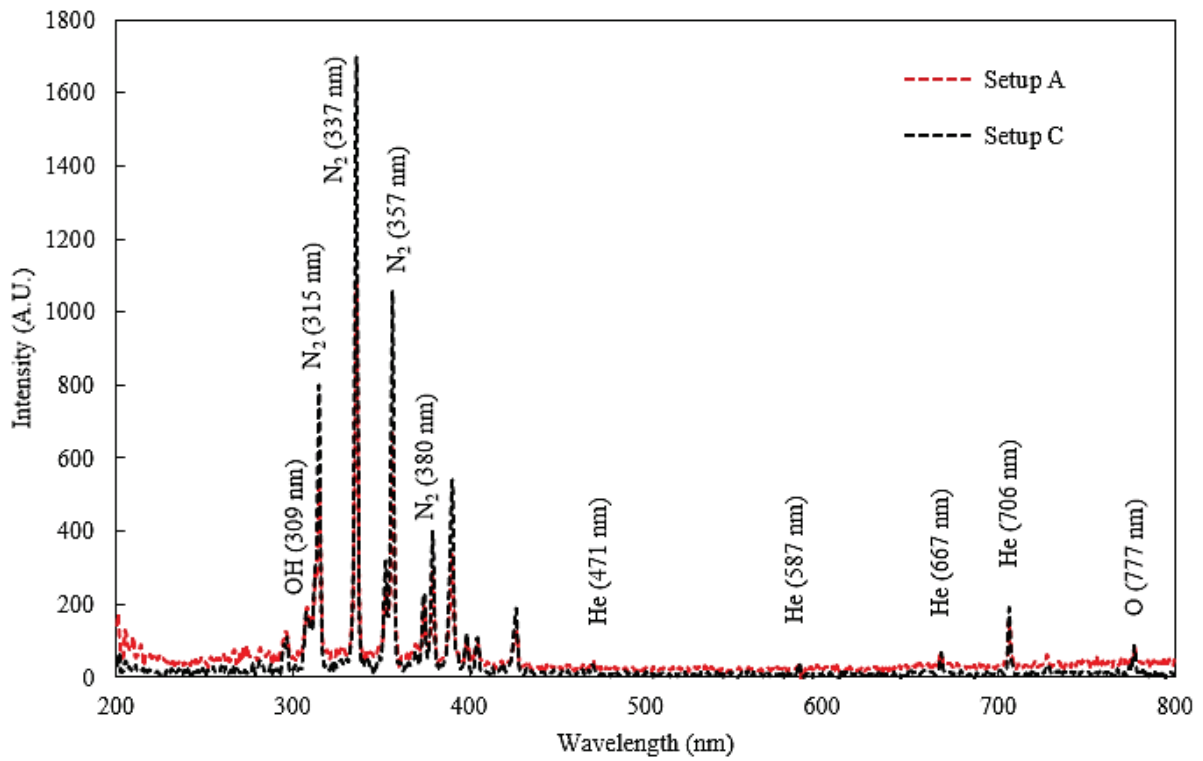


Fig. 9: Optical emission spectroscopies of APPJ generated from setups A and C at 9 mm below the plasma nozzle

Table 1: Combinations of electrode polarities and APPJ observation

Set up	Polarity of the electrode (GND: Ground Voltage, HV: High Voltage waveform)			Observation of APPJ
	Electrode 1	Electrode 2	Electrode 3	
A	GND	HV	GND	Longer APPJ (~ 4 – 5 cm)
B	GND	HV	HV	Smaller APPJ (~ 1 cm)
C	HV	GND	HV	Longer APPJ (~ 4 – 5 cm)
D	HV	GND	GND	Smaller APPJ (~ 1 cm)

As shown in figure 9, both the spectroscopies are identical to each other. However, setup C shows a strong concentration of radicals compare to the setup A. Also, both the spectroscopies detect the surface modifying radicals such as, OH, N₂, and O.

3.3 Surface modification of bio-compatible material and adhesion of hiPSCs

As the setups A and C generate longer APPJs, it was experimented with the modifying the PDMS surfaces. Spin-coated PDMS surfaces were irradiated to the APPJs and the irradiated surfaces were stained with the RhodamineB for estimating the wetting sizes (the procedure explained under section 2.3). Figure 10 shows the comparison of the wetting area sizes against the irradiation time for the setups A and C.

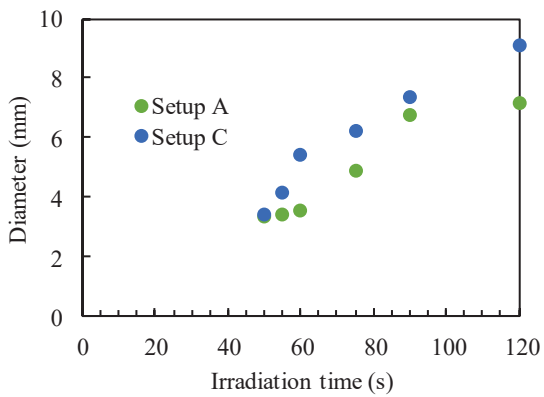


Fig. 10: Comparison graph of the estimated wetted area against the irradiation time for setups A and C using RhodamineB test

As shown in figure 10, wetting area sizes are increased with the increases of the irradiation time. Setup C generates larger wetting area comparing to the setup A for the same irradiation time.

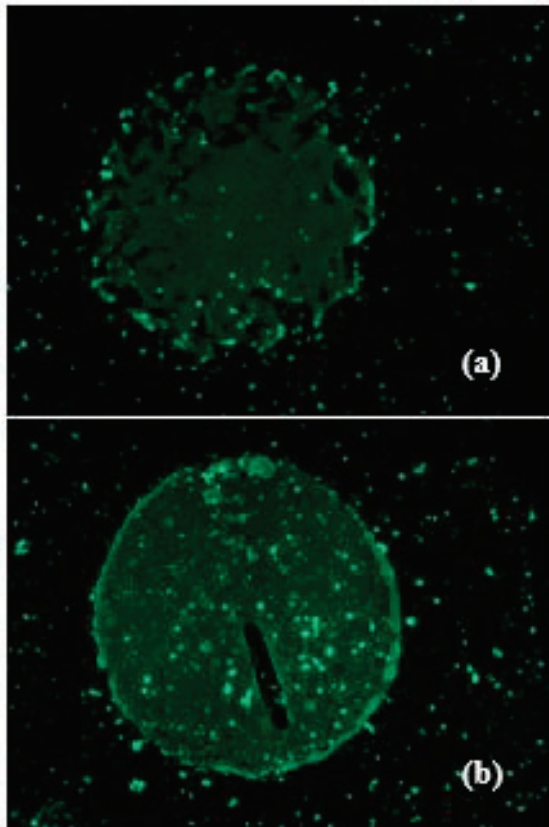


Fig. 11: Fluorescence images of the calcine induced hiPSCs after two days of seeding to modified PDMS surface; (a) Setup A and (b) Setup C

For the further analysis irradiated PDMS surfaces were stained with the calcine induced hiPSCs and were observed in the behavior after two days. Initial observation shows hiPSCs adhere to the modified PDMS surfaces and generate patterning if the irradiation time 120 s or above. Below this limit stained hiPSCs shows non-adherence to the PDMS surfaces or non-patterning.

Figure 11 shows the calcine induced fluorescence images of the hiPSCs after two days of seeding for 120 s irradiated PDMS surfaces for setups A and C. Experimental analysis shows irradiated surface using setup C (Fig.11 (b)) tend to strongly adhere and pattern hiPSCs compare to surface modification done by setup A (Fig.11 (a)).

4. Conclusions

This study performs the alternative approach to modify the bio-compatible surface using the APPJs compare to conventional low-pressure plasma. Double electrode configured APPJs generate longer APPJ while the addition of extra electrode can use to minimize the reflection effect and maximize plasma jet. Polarity variances in double electrodes and additional electrode generate different sizes of APPJ. Modified PDMS surface area increases with the increase of irradiation time and 120 s or above irradiated PDMS surfaces are suitable for the stain and grow hiPSCs in laboratory conditions.

References

- [1] J.A. Thompson, J. Itskovitz-Eldor, S.S. Sharpio, M.A. Waknitz, J.J. Swiergiel, V.S. Marshall, and J.M. Jones, "Embryonic Stem Cell Lines Derived from Human Blastocysts," *Science*, vol. 282, pp. 1145-1147, 1998.
- [2] K. Takahashi, K. Tanabe, M. Ohnuki, M. Narita, T. Ichisaka, K. Tomoda, and S. Yamanaka,

- "Induction of pluripotent stem cells from adult human fibroblasts by defined factors," *Cell*, vol. 131, no. 5, pp. 861-872, 2007.
- [3] J. Byrne, "Overcoming clinical hurdles for autologous pluripotent stem cell-based therapies," *OA Stem Cells*, 2013.
- [4] J. El-Ali, P. K. Sorger, and K. F. Jensen, "Cells on chips," *Nature*, vol. 442, no. 7101, pp. 403-411, 2006.
- [5] K. Gupta, D.H. Kim, D. Ellison, C. Smith, A. Kundu, J. Tuan, K.Y. Suh, and A. Leychenko, "Lab-on-a-chip devices as an emerging platform for stem cell biology," *Lab. Chip*, vol. 10, no. 16, pp. 2019-2031, 2010.
- [6] D.C. Duffy, J.C. McDonald, O.J.A. Schuller, and G.M. Whitesides, "Rapid Prototyping of Microfluidic Systems in Poly(dimethylsiloxane)," *Analytical Chemistry*, vol. 70, no. 23, pp. 4974-4984, 1998.
- [7] J. Zhou, A.V. Ellis, and N.H. Voelcker, "Recent developments in PDMS surface modification for microfluid devices," *Journal of Electrophoresis*, vol. 31, no. 1, pp. 2-16, 2010.
- [8] R. Yamada, K. Hattori, M. Tagaya, T. Sasaki, D. Miyamoto, K. Nakazawa, S. Sugiura, T. Kanamori, and K. Ohnuma, "Plasma-Patterned Polydimethylsiloxane Surface With Single-Step Coating with a Mixture of Vitronectin and Albumin Enables the Formation of Small Discs and Spheroids of Human Induced Pluripotent Stem Cells," *Journal of Plasma Medicine*, vol. 4, no. 1-4, pp. 165-176, 2014.
- [9] R. Yamada, K. Hattori, Motohiro Tagaya, T. Sasaki, S. Sugiura, T. Kanamori, and K. Ohnuma, "Control of adhesion of human induced pluripotent stem cells to plasma-patterned polydimethylsiloxane coated with vitronectin and gamma-globulin," *Journal of Bioscience and Bioengineering*, vol. 118, no. 3, pp. 315-322, 2014.
- [10] K. Ohnuma, A. Fujiki, K. Yanagihara, S. Tachikawa, Y. Hayashi, Y. Ito, Y. Onuma, T. Chan, T. Michiue, M.K. Furue, and M. Asashima, "Enzyme-free Passage of Human Pluripotent Stem Cells by Controlling Divalent Cations," *Scientific Reports*, 2014.
- [11] W.T.L.S. Fernando, K. Morito, G. Kato, K. Ohnuma, K. Takahashi, T. Sasaki, and T. Kikuchi, "Effect of the additional ground electrode in double electrode configuration in maintaining stable atmospheric pressure plasma jet for bio-applications," in *Cheminas37*, Tsukuba, Japan, 2018.
- [12] W. Rasband, "ImageJ," U. S. National Institutes of Health, Bethesda, Maryland, USA, 1997-2019. [Online]. Available: <https://imagej.nih.gov/ij/>.

AC glow discharge in liquids: the transfer of charged particles and the ability to noble metal nanoparticle synthesis

Thai Van Phuoc, S. Abe, K. Kosugi, N. Saito, K. Takahashi, T. Sasaki, and T. Kikuchi

Nagaoka University of Technology, 1603-1 Kamitomioka, Nagaoka, Niigata 940-2188, Japan

ABSTRACT

In this work, we investigated the influence of alternating current glow discharge in liquids. The change of pH values in solutions of deionized water, sodium hydroxide, nitrate-salt were recorded to study the transfer of charged particles from the discharge into liquids. We found that deionized water and sodium solutions were acidified during the discharge, in contrast, nitrate-salt solutions were alkalized. Alternating current glow discharge generated both free electrons and positive ions in liquids that lead to completely change in chemical compositions. Our results also indicated that silver and gold nanoparticles were successfully formed by the discharge. The synthesized nanoparticles are mainly generated at the area of 10 nm below the plasma-liquid interface.

Keywords

Key Words: AC glow discharge, charged particles, silver, gold, nanoparticle synthesis

1. Introduction

Noble metal nanoparticles such as gold, silver have been widely employed in many applications from biomedical engineering[1] to catalyst[2] and electronic conductor[3] because of their unique properties[4] [5]. There are many ways to synthesize these noble nanoparticles such as microwave[6], laser method[7], and biosynthesis[5]. However, these methods have some disadvantages related to environmental risk, the degree of purity. Therefore, their synthesis methods have been continuously studied to improve the degree of purity at high synthesis productivity.

Plasma-liquid interaction has been studied as a useful tool for nanomaterial production. Nanoparticles can be directly generated via the reductions between free electrons from plasma and metallic cations in liquids[8]. There have many studies to investigate the effect of particles from plasma on liquids[8]–[11]. Generation and configuration of plasma-liquid interaction have been investigated to broaden its applications[12]. However,

these studies have been mainly focused on using a direct current supply power to generate plasma[8], [9]. The properties of alternating current (AC) glow discharge in liquids have been not considered.

In this work, we investigated the transfer of charged particles from an AC glow discharge in liquids. The ability of metallic nanoparticle was also studied.

2. Experimental Setup

AC glow discharge was generated in liquid as shown in Fig. 1. The experimental setup in this study is similar to the setup used in Ref. [13]. A glass beaker ($\varnothing 53 \times 70$ mm) including 100 mL of a solution was put on an aluminum plate connected to ground. A copper tube (4 mm of inner and 6mm of outer diameters, respectively) was connected to a supply power as the anode electrode. The supplied voltage and frequency were 18 kV and 38kHz, respectively. Voltage and current waveforms were measured using a high voltage probe and an oscilloscope as described in Ref. [13]. Helium gas fed to anode electrode was maintained at 5 L/min.

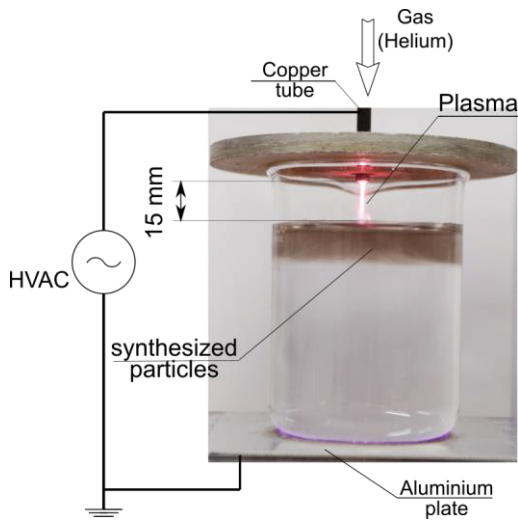


Fig. 1 Experimental setup

Solutions of sodium nitrate (NaNO_3), sodium hydroxide (NaOH), deionized water (H_2O), silver nitrate (AgNO_3), tetrachloroauric acid (HAuCl_4) were used to study the influence of AC glow discharge in liquid. The pH/EC values in these solutions were monitored to observe the chemical composition change in liquid during the discharge.

The synthesized particles in solutions of AgNO_3 or HAuCl_4 were characterized on TEM (HT7700 Hitachi) at 100 kV of accelerating voltage.

3. Results and Discussion

3.1 Effect of AC discharge in liquids

Table 1 shows the pH change in solutions during the discharge. It was determined that AC glow discharge acidifies neutral and hydroxide solutions, in contrast, alkalizes nitrate-salt solutions. In the case of H_2O , pH value was dropped and stabilized at 4.0 within 4 minutes of discharge. pH value in 0.2 mM NaOH was continuously decreased from 10.4 to 8.7 after 10 minutes of discharge. Specially, pH values in 2.5 mM NaNO_3 solution were decreased following by increasing.

Tochikubo et al.[9] reported that the transfer of the charged particles from plasma on liquid causes pH change in solutions. In detail, electrons at low energy level (a few eV) from plasma quickly solvate in liquid and become hydrated electrons (e_{eq}). Subsequently, these e_{eq} react with surrounding water molecules as reactions (1) and (2) [9] to generate hydroxide cations (OH^-). This leads to increase in pH

value of solutions.



In contrast, the interactions between the positive ions from plasma and water molecules as reactions (3) and (4) [9] result in generating H^+ (H_3O^+). This causes pH increase in solutions.



where, X^+ denotes the positive ion from plasma.

In this study, an AC supply power was used to generate the plasma on liquid. The electric field is alternately reversed after each half of period $T=1/f$, where f is the frequency of the supplied power (in this study $f = 38$ kHz). Therefore, the charged particles transferring from plasma into liquids include both free electrons and positive ions. These charged particles alternately impact on a liquid in a period T . For that reason, the pH change in solutions under AC glow discharge is resulted in the total productions impacted by both positive ions and electrons.

Table 1. The pH values in solutions for 0, 5, and 10 minutes of the discharge

	pH value		
	0 min	5 min	10 min
0.2mM NaOH	10.4	8.8	8.7
H_2O	6.5	3.9	3.9
2.5mM NaNO_3	5.5	4.8	8.7
25mM AgNO_3	5.4	5.73	7.2

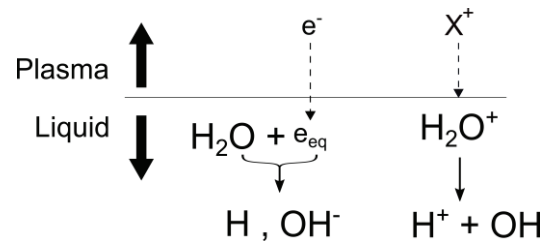


Fig. 2 Schematic of transfer of charged particles from AC glow discharge in liquid

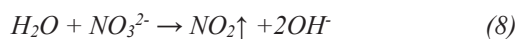
One hydrated electron can quickly neutral one H^+ ion into water molecules as reaction (5) or via reactions (1), (2), and (6). Therefore, the pH decreases in solutions of H_2O and 0.2 mM NaOH

indicated that the concentration of e_{eq} generated by AC glow discharge in liquids is smaller than the concentration of H^+ .



The reasons for the difference in concentration of H^+ compared to e_{eq} could be explained as follows. Because AC glow discharge was generated at atmospheric pressure, the energy of free electrons is a few eV. Therefore, all e_{eq} stay in the area of 10 nm below the plasma-liquid interface. It takes a time for these e_{eq} react with surrounding water molecules. This leads to a portion of e_{eq} pulled out of the liquid's surface when the electric field was reversed after $T/2$. In contrast, almost H^+ ions are neutralized as discussed above or quickly diffuse into the bulk liquid.

In the case of nitrate-salt solutions, there occur the stepwise reactions (7) and (8) [14] between NO_3^- and e_{eq} to generate OH^- ions. Note that the combination between one NO_3^- and one e_{eq} could procedure two OH^- ions. This leads to the concentration of OH^- ions higher than H^+ . However, the rate constant of reaction (8) is $1.0 \times 10^5 \text{ s}^{-1}$ (first order) [14]. It is not fast enough to procedure OH^- ions with a concentration that can neutralize all H^+ ions generated by positive ions in each $T/2$. It takes time to fully complete the reaction (8). This explains the reason why the pH value of 2.5mM $NaNO_3$ solution was decreased from 5.5 to 4.8 alkaline for 5 minutes of discharge, then increased again to 8.7 after 10 minutes of discharge.



3.2. Noble metal nanoparticle synthesis

Our result indicates that silver and gold nanoparticles are synthesized by AC glow discharge. Figure (3) illustrates the TEM images of silver nanoparticles synthesized (AgNPs) in 5mM $AgNO_3$ after 10 minutes of discharge. The image shows that the shape of AgNPs is typically spherical.

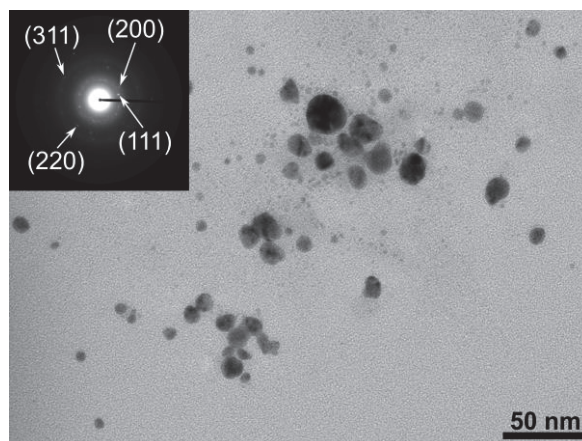


Fig. 3 TEM image of AgNPs synthesized in 25mM $AgNO_3$ solution after 10 minutes of the discharge

The formation mechanism of silver nanoparticles in bulk liquids has been studied. The process starts the formation of silver nuclei following by the growth of these nuclei in nanoscale. It is easy to form silver nuclei under AC glow discharge via reactions (9) or (10) [14]:



The reaction (9) could be inhibited by another electron scavengers such as H^+ , NO_3^- . In the solution of 25mM $AgNO_3$, e_{eq} not only react Ag^+ but also with NO_3^- to generate OH^- ions. This explains the reason the pH value of 25mM $AgNO_3$ was increased to 7.2 after 10 minutes of discharge as shown in Table 1.

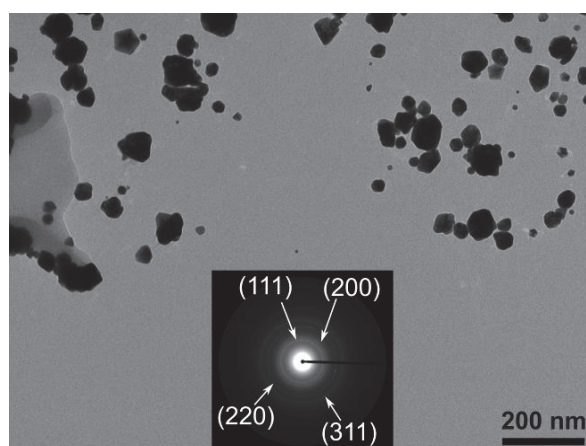


Fig. 4 TEM image of AuNPs synthesized in 0.05 mM $HAuCl_4$ solution after 10 minutes of the discharge

We also determined that gold nanoparticles (AuNPs) can be synthesized in HAuCl₄ solution. Figure 4 shows the TEM image of gold nanoparticle in the solution of 0.05mM HAuCl₄ after 10 minutes of discharge. The gold nuclei were formatted via the reaction (11) [14]:



Note that all e_{eq} stay in the area of 10 nm below the plasma-liquid interface. Therefore, AgNPs and AuNPs are mainly formed in this area and then diffuse into the bulk liquids as shown in Fig. 1.

4. Conclusions

In this work, we studied the influence of AC glow discharge in liquids. We found that AC glow discharge generates both positive ions and electrons in liquids which leads to change the chemical composition in solution. It is determined that AC glow discharge can be used for noble metal nanoparticles.

References

- [1] P.-C. L. Zhenjiang Zhang, “zhang2018.pdf,” A. S. H. M. Ahmed Barhoum, Ed. Elsevier, 2018, pp. 177–233.
- [2] M. R. Luo, *Encyclopedia of Color Science and Technology*. 2016.
- [3] S. Suresh, “Semiconductor Nanomaterials, Methods and Applications: A Review,” *Nanoscience and Nanotechnology*, vol. 3, no. 3, pp. 62–74, 2013.
- [4] G. Schmidl *et al.*, “Formation and characterization of silver nanoparticles embedded in optical transparent materials for plasmonic sensor surfaces,” *Materials Science and Engineering B: Solid-State Materials for Advanced Technology*, vol. 193, no. C, pp. 207–216, 2015.
- [5] M. R. Bindhu and M. Umadevi, “Antibacterial and catalytic activities of green synthesized silver nanoparticles,” *Spectrochimica Acta - Part A: Molecular and Biomolecular Spectroscopy*, vol. 135, pp. 373–378, 2015.
- [6] C. He, L. Liu, Z. Fang, J. Li, J. Guo, and J. Wei, “Formation and characterization of

- silver nanoparticles in aqueous solution via ultrasonic irradiation,” *Ultrasonics Sonochemistry*, vol. 21, no. 2, pp. 542–548, 2014.
- [7] B. Tangeysh, K. M. Tibbetts, J. H. Odhner, B. B. Wayland, and R. J. Levis, “Gold Nanoparticle Synthesis Using Spatially and Temporally Shaped Femtosecond Laser Pulses: Post-Irradiation Auto-Reduction of Aqueous [AuCl₄]⁻,” 2013.
- [8] N. Shirai, S. Uchida, and F. Tochikubo, “Synthesis of metal nanoparticles by dual plasma electrolysis using atmospheric dc glow discharge in contact with liquid Synthesis of metal nanoparticles by dual plasma electrolysis using atmospheric dc glow discharge in contact with liquid,” vol. 046202, no. 2011, p. 54010, 2014.
- [9] F. Tochikubo, Y. Shimokawa, N. Shirai, and S. Uchida, “Chemical reactions in liquid induced by atmospheric-pressure dc glow discharge in contact with liquid Chemical reactions in liquid induced by atmospheric-pressure dc glow discharge in contact with liquid,” *Japanese Journal of Applied Physics*, vol. 126201, no. February 2016, pp. 0–8, 2014.
- [10] N. Shirai, K. Ichinose, S. Uchida, and F. Tochikubo, “Influence of liquid temperature on the characteristics of an atmospheric dc glow discharge using a liquid electrode with a miniature helium flow,” *Plasma Sources Science and Technology*, vol. 20, no. 3, 2011.
- [11] S. U. Fumiyoshi Tochikubo, “Simulation of Glow-Discharge Electrolysis at Atmospheric Pressure for Silver Nanoparticle Synthesis in Liquid,” *Plasma conference 2017*, no. 3, pp. 5–6, 2017.
- [12] P. J. Bruggeman *et al.*, “Plasma-liquid interactions: A review and roadmap,” *Plasma Sources Science and Technology*, vol. 25, no. 5, 2016.
- [13] T. Van Phuoc *et al.*, “Synthesis Silver Nanoparticles via Reduction Reaction by AC Glow Discharge at Atmospheric Pressure with Liquid,” 2018, pp. 60–62.
- [14] “NIST Solution Kinetics Database.”

Research on Primary Streamer Propagation Characteristics of Nanosecond Pulsed Discharge in Coaxial Electrode

Terumasa Ryu*1, Hitoshi Yamaguchi1, Douyan Wang2, and Takao Namihira2

**Graduate School of Science and Technology, Kumamoto University1*

Institute of Pulsed Power Science, Kumamoto University2

ABSTRACT

Non-thermal plasma has been actively studied for industrial and environmental applications. The observation of discharge plasmas is beneficial for better understanding of the plasma physics of this growing field. It is well known that a streamer head always has the largest electric field during discharge entire process. Furthermore, the streamer head produces a variety of radical species according to feeding gas with high efficiency. Here, general pulsed discharge with a pulse duration of 100s ns is mainly divided into two phases, one is the primary streamer discharge and the other is secondary streamer discharge. In the recent study, a nanosecond pulsed power generator which can generate a pulsed voltage with 5 ns of duration was developed and achieved a higher efficiency on ozone generation, NO removal, and water cleaning. However, the underlying mechanisms of these high efficiencies are not well understood. The present study investigated the effects of electrode geometry in and gas composition into coaxial electrode on the streamer discharge. In the experiments, the primary streamer propagation process was observed using a high speed gated ICCD camera and time-resolved spectroscopic.

Keywords

Pulsed Power, Nanosecond Pulse, Primary Streamer Discharge, Inner Diameter of Electrode, Gas Composition

1. Introduction

Recently, pulsed discharge plasma has been widely used in many applications such as ozone generation, gas treatment, and water cleaning [1-8]. Due to the fast electrons that are generated by high voltage pulses, they are very efficient in producing highly reactive radical species and energetic photons. These products can consequently react with, for instance, particles in gas streams (e.g. pollutants, odor and dust), contamination in water. Typically, general pulsed discharge with a pulse duration of 100s ns is mainly divided into two phases, one is a primary streamer discharge and the other is a secondary streamer discharge. The tip of primary streamer discharge, which is called the streamer head, in particular, contributes to radical production. In the recent study, Namihira and Wang et al. developed a nanosecond (ns) pulsed power generator with a pulse duration of 5 ns

and then improves energy transmission efficiency due to very little loss by heating of gas by shifting to secondary streamer discharge only a little. Therefore, ns pulsed discharge has much higher treatment efficiency than that of general pulsed discharge [9-11]. However, the underlying mechanisms of these high efficiencies are not well understood. Further understanding of the characteristics of ns pulsed discharge is of great importance in order to increase the ozone concentration and improve other treatment performance.

In this research, the present study investigates the effects of inner diameter in and gas composition into coaxial electrode on primary streamer discharge by observing the propagation characteristics of nanosecond pulsed discharge. In addition, the applied reduced electric field strength of primary streamer was qualitatively estimated from the ratio of intensities of

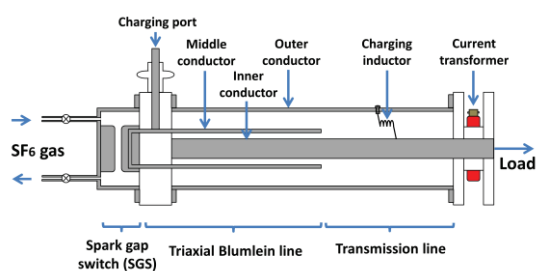


Fig. 1 Schematic diagram of the ns pulse generator.

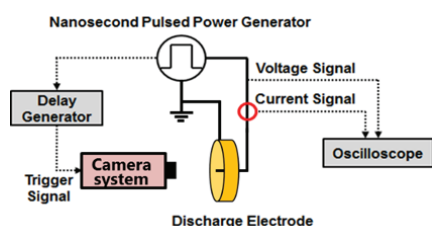


Fig. 2 Schematic diagram for imaging system of the pulsed discharge.

the spectral bands corresponding to transitions second positive system (SPS) of nitrogen molecule N_2 and that of the first negative system (FNS) of the ionized molecule N_2^+ .

2. Experimental Setup

2.1 Nanosecond pulse generator

Figure 1 shows the schematic diagram of the ns pulsed power generator used in the present work. The ns pulse generator consisted of a coaxial high-pressure spark gap switch (SGS) as a low-inductance self-closing switch, a triaxial Blumlein line as the pulse-forming line, and a pulse voltage transmission line which transmits energy from the triaxial Blumlein line to the load. The SGS was filled with SF_6 gas, whose pressure variation allows regulation of the generator's output voltage. The gas distance was fixed at 1 mm. The triaxial Blumlein line consisted of an inner rod conductor, a middle cylinder conductor, and an outer cylinder conductor. All the conductors were placed concentrically. The outer conductor was grounded, and the inner and outer conductors were connected through a charging inductor. The triaxial Blumlein line and transmission line were filled with silicon oil as an insulation and dielectric medium. The calculated unit inductance and capacitance of the triaxial Blumlein

line were 140 nH/m and 216 pF/m, respectively, by which the characteristic impedance was calculated at 50 ohm. The length of the triaxial Blumlein line was 500 mm and the calculated pulse duration of the triaxial Blumlein line was 5 ns.

2.2 Imaging system for pulsed discharge observation

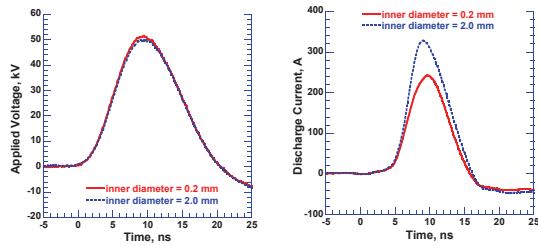
Figure 2 shows a schematic diagram for imaging of the pulsed discharge. The ns pulse generator was used to generate the ns pulsed discharge. A high-speed gated ICCD camera was used to observe the framing images of streamer heads in the discharge electrode. The exposure time of the ICCD camera was fixed at a certain sub-ns. A time-resolved spectroscope which is combined spectroscope with streak camera was used to observe the continuous spectral intensity with ultra-fast and time-resolution of the ns pulsed streamer discharge. The sweep time and grating were fixed at 10 ns and 600 gr/mm, respectively. The slit width of spectroscope was fixed at 0.1 μm and the that of the streak was adjusted maximum 17 mm to observe the intensity of streamer head which propagates between electrodes. Also, the ICCD camera and time-resolved spectroscope were synchronized with the generator through a delay generator. A concentric coaxial cylindrical reactor was employed as the discharge electrode. A rod made stainless steel was placed concentrically within a copper cylinder. The cylinder electrode was grounded, and its diameter was 60 mm. A short length of the electrode, 15 mm in length, was necessary to render a clear image of the streamer heads. To investigate the effects of inner diameter in and gas composition into a coaxial electrode, every two kinds of the parameter, 0.2 mm and 2.0 mm in diameter under air, nitrogen (N_2) and air gas under the condition of 1 mm in diameter, respectively, were used in this research. The gas mass flow rate was fixed at 4.0 L/min at atmospheric pressure using mass flow controller. For all experiments, a positive voltage from ns pulse generator was applied to the central rod electrode and was measured using a capacitive voltage divider. The discharge current through the coaxial electrode was measured using a current transformer, which was located just before the electrode. A digital

oscilloscope with a maximum bandwidth of 4 GHz and a maximum sample rate of 20 Gsamples/sec recorded the signals from the capacitive voltage divider and the current transformer.

3. Results and Discussion

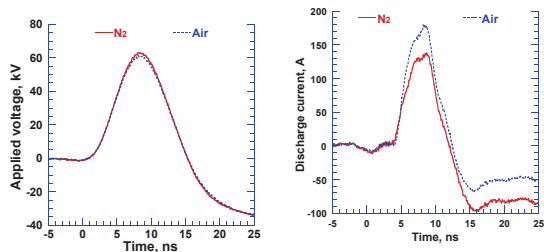
3.1 Waveform analysis

Figure 3 shows typical waveforms of the applied



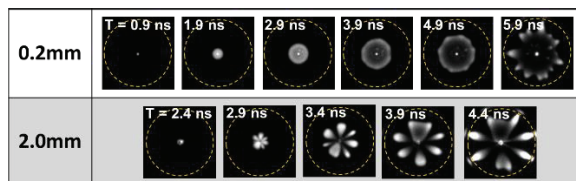
(a) Applied voltage (b) Discharge current

Fig. 3 Typical waveforms of applied voltage and discharge current (fixed at air gas).

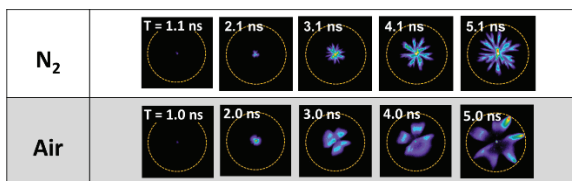


(a) Applied voltage (b) Discharge current

Fig. 4 Typical waveforms of applied voltage and discharge current (fixed at 1 mm in diameter).



(a) Different inner diameter



(b) Different gas composition

Fig. 5 Framing images of the ns pulsed discharge.

voltages to (a) and discharge current into (b) the coaxial electrode in different inner diameter. The output voltage from the ns pulse generator was applied at 0 ns. Moreover, Fig. 4 also represents typical waveform in different gas composition similar to Figure 3. It is confirmed from Figure 3 and Figure 4 that discharge current hardly flow during primary streamer. This is because that the capacitance between streamer head and outer cylindrical electrode might work the current limiting impedance during propagating. Subsequently, Streamer heads with a higher density of ionization reached grounded cylinder electrode, and subsequently, the secondary streamer discharge connects between electrodes with higher conductivity plasma channel.

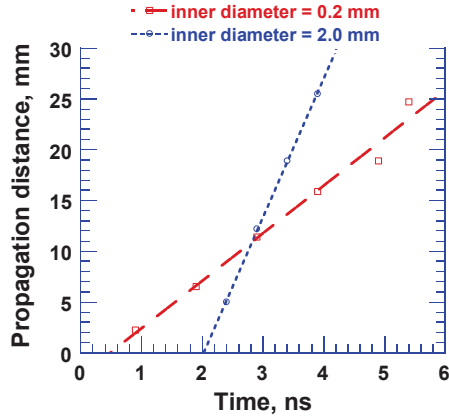
3.2 Propagation behavior of streamer heads

Figure 5 show framing images of emissions from streamer discharges as a function of time in different inner diameter (a) and gas composition (b), respectively. Brightness degree reflects the emission intensity. In the experiments, all images were photographed using the identical gain of the ICCD camera. Here, T ns of each image indicates the onset time of streamer head formation in the vicinity of the central rod electrode after the application of pulse voltage ($T = 0$ ns) and this corresponds to the horizontal axis in Figure 3 and 4. Also, time above each image indicate the onset time of camera exposure. From Figure 5, the streamer heads propagate from the central rod to the grounded cylinder in all directions of the coaxial electrode. Here, a significant difference in the propagation process on the streamer heads was observed between each parameters. In different inner diameter from Figure 5 (a), it is confirmed that more orbicular streamer heads under the inner diameter of 2.0 mm progress between electrodes than the inner diameter of 0.2 mm. This is considered because the streamer head generated under the condition of 2.0 mm has a higher electric field than that of the thin diameter, and therefore the streamer heads repel each other more strongly. Also, under the condition of N₂ gas as shown Figure 5 (b), streamer heads were branched more frequently in a zigzag fashion, and their diameter was smaller during its propagation. In

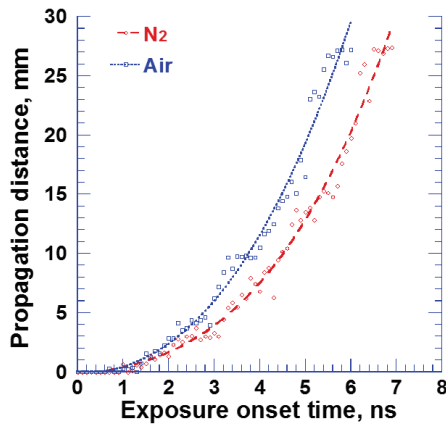
contrast, under air gas condition, the streamer heads were not branched, and their diameter was much larger.

3.3 Propagation velocity of streamer heads

Streamer head positions relative to the central rod electrode as a function of time were determined by images shown in Figure 5. The time dependences of



(a) Different inner diameter



(b) Different gas composition

Fig. 6 Time dependence of streamer head position from central rod electrode.

Table I Streamer onset characteristics in different parameters

	Inner diameter		Gas composition	
	0.2	2.0	N ₂	Air
Average propagation velocity, mm/ns	4.8	12.5	5.2	5.9
Applied voltage, kV	2.6	7.2	4.2	3.3
Electric field concentration factor f	52.4	8.5	14.4	14.4

streamer head position for different inner diameter gas composition are shown in Figure 6 (a) and (b). Furthermore, a summary of the applied voltage to the central rod electrode at the onset times of the streamer head formation was shown in Table I. The electric field concentration factor was calculated using Eq. (1), where that R_1 and R_2 are central wire radius and grounded cylinder radius respectively.

$$f = (R_2/R_1 - 1) / \ln R_2/R_1 \quad (1)$$

As shown Figure 6, the streamer heads were generated near the central rod electrode and then propagated toward the grounded cylinder electrode. The average velocity of streamer head was approximated from inclinations between 0 mm and 30 mm of positions from the central rod electrode and includes in Table I. From Table I, the onset time of the propagation velocity under 0.2 mm and 2.0 mm in diameter was the significant difference due to electric field concentration factor f (0.2 mm = 52.4, 2.0 mm = 8.5), which determines easiness of discharge onset. Consequently, it needs to apply higher voltage amplitude for streamer heads to initiate those progress from central rod electrode under the thicker diameter. On the other hand, in different gas compositions, propagation onset times was the similar value in order to same electric field concentration factor f (1 mm = 14.4). However, the velocity under air gas is a little bit faster than that of N₂ gas as shown Table I. This is explained by UV photon from N₂ and photoionization of O₂ [12]. Under the condition of N₂/O₂ mixed gas, a UV photon provided by excited nitrogen molecule leads to photoionization of the oxygen molecule, which results in the production of new free electron. Moreover, the new free electron produced is accelerated by the electric field and then is excited new nitrogen molecule again. Thereby, it is considered that the streamer head is progressed by the interaction of the photochemical cycle between nitrogen and oxygen molecules.

In general, it is known by the simulation works [13, 14] that the electric field strength of streamer heads is reflected in its propagation velocity. In this paper, the

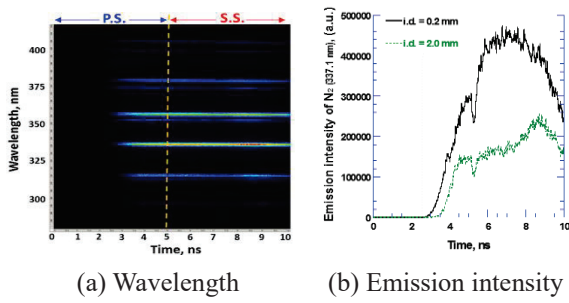


Fig. 7 Time dependence of wavelength and emission intensity.

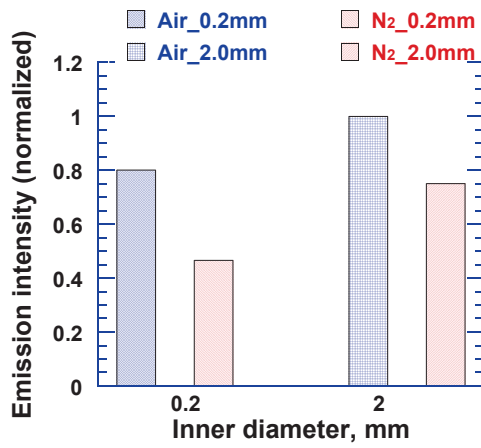


Fig. 8 Qualitative $R_{391/337}$ dependence of the inner diameter and gas composition.

amount for the attraction force of electron avalanches into high electric field region of the streamer head contributes to its electric field strength and thereby might be caused the increment of propagation velocity. In order to clarify this relationship between electric field strength and propagation velocity, investigated as follows.

3.4 Qualitative estimation of reduced electric field

To estimate qualitative reduced electric field strength, optical emission spectroscopy was used. A spectroscopic measurement based on the measurement of the intensity ratio of nitrogen molecules from the ground state by the electron impact is the dominant process in the plasma. Usually, the intensity of the most intensive spectral band of the second positive system (SPS) of nitrogen molecule N_2 and that of the first negative system (FNS) of the ionized molecule N_2^+ are compared. The wavelengths of these band heads are 337.1 nm and 391.4 nm, respectively. We

donate below the ratio of the intensities of these bands by $R_{391/337}$. For determination of the field strength, the ratio $R_{391/337}$ must be known as a function of the electric field strength [15]. Figure 7 (a) shows the time dependence of the wavelength from nitrogen molecule and Figure 7 (b) represents the emission intensity analyzed as an example from SPS (337.1 nm) of Figure 7 (a), respectively. Here, from figure 5, primary streamer can reach outer electrode at roughly 5 ns from the voltage application onset. Therefore, in the experiment, qualitative $R_{391/337}$ was estimated from integrated value from 0 ns to 5 ns as shown Figure 7 (b). Figure 8 shows qualitative $R_{391/337}$ dependence of the inner diameter and gas composition. It is confirmed that Fig. 5 that thicker diameter under same gas composition measured the higher quantitative $R_{391/337}$. Moreover, under same inner diameter, quantitative $R_{391/337}$ in air gas condition is larger value than that of N_2 gas. As the results, the propagation velocity of primary streamer heads which calculated from framing image correlated with qualitative $R_{391/337}$.

4. Conclusions

In this paper, the effects of inner diameter and gas composition on the propagation process of a 5 ns pulsed primary streamer discharge was investigated using an ICCD camera and time-resolved spectroscopy. Results are summarized as follows.

- Propagation velocity of streamer heads is faster under thicker diameter and air gas than thinner diameter and N_2 gas.
- Qualitative $R_{391/337}$ value, which determines applied reduced electric field strength, is correlated with the propagation velocity of streamer heads.

Therefore, by estimating “quantitative” $R_{391/337}$, it is expected to clarify the further propagation process in detail.

References

- [1] S. Samukawa et al., “The 2012 plasma roadmap”, *J. Phys. D, Appl. Phys.*, **45**, 25, p.253001 (2012).

- [2] T. Namihira et al., “Improvement of NO_x removal efficiency using short-width pulsed power”, *IEEE Trans. Plasma Sci.*, **28**, pp. 434–442 (2000).
- [3] D. Wang et al., “Dependence of NO_x removal by pulsed streamer discharge on the input energy density to nitric oxide ratio”, *J. Advanced Oxidation Technologies*, **8**, 2, pp.248–254 (2005).
- [4] A. Komuro et al., “Behaviour of OH radicals in an atmospheric-pressure streamer discharge studied by two-dimensional numerical simulation”, *J. Phys. D, Appl. Phys.*, **46**, p.175206 (2013).
- [5] F.J.C.M. Beckers et al., “Pulsed corona demonstrator for semi-industrial scale air purification”, *IEEE Trans. Plasma Sci.*, **41**,10, pp. 2920–2925 (2013).
- [6] W.F.L.M. Hoeben et al., “Oxidative degradation of toluene and limonene in air by pulsed corona technology”, *J. Phys. D, Appl. Phys.*, **45**, 5, p. 055202 (2012).
- [7] J.S. Clements et al., “Combined removal of SO₂, NO_x, and fly ash from simulated flue gas using pulsed streamer corona”, *IEEE Trans. Plasma Sci.*, **25**, 1, pp. 62–69 (1989).
- [8] F.J.C.M. Beckers et al., “Low-level NO_x removal in ambient air by pulsed corona technology”, *J. Phys. D, Appl. Phys.*, **46**, 29, p. 295201 (2013).
- [9] D. Wang et al., “Pulsed Discharge Induced by Nanosecond Pulsed Power in Atmospheric Air”, *IEEE Trans. Plasma Sci.*, **38**, 10, pp. 2746–2751 (2010).
- [10] T. Matsumoto et al., “Performances of nanoseconds pulsed discharge”, *Acta Phys. Pol. A*, **115**, 6, pp.1101–1103 (2009).
- [11] D. Wang et al., “Recent Progress of Nano-Seconds Pulsed Discharge and its Applications”, *J. Advanced Oxidation Technologies*, **14**, 1, pp.131–137 (2011).
- [12] T. Ryu et al., “Influence of Nitrogen/Oxygen Gaseous Ratio on Nanosecond Pulsed Discharge Behavior”, *Proc. 7th Euro-Asian Pulsed Power Conf. 8*, *IEEE*, pp.206–209 (2019).
- [13] F. Tochikubo et al., “Numerical simulation of streamer propagation and radical reactions in positive corona discharge in N₂/NO and N₂/O₂/NO”, *Jpn. J. Appl. Phys.*, **41**, pp. 844–852 (2002).
- [14] A. Komuro et al., “Numerical simulation for the production of chemically active species in primary and secondary streamers in atmospheric-pressure dry air”, *J. Phys. D, Appl. Phys.*, **48**, p. 215203 (2015)
- [15] P. Paris et al., “Intensity ratio of spectral bands of nitrogen as a measure of electric field strength in plasmas”. *J. Phys. D: Appl. Phys.*, **38**, 21, pp.3894–3899 (2005).

Effect of oxygen concentration on ethylene decomposition by nanosecond pulsed discharge

Yasuaki Torigoe¹, Asuki Iwasaki¹, Douyang Wang², Takao Namihira²

¹*Graduate School of Science and Technology, Kumamoto University, Japan*

²*Institute of Pulsed Power Science, Kumamoto University, Japan*

ABSTRACT

Ethylene (C₂H₄) is a kind of plant hormone. The ethylene was decomposed by the nanosecond pulsed discharge. The applied voltage from the nanosecond pulse generator to the coaxial cylinder type reactor was adjusted into 40 kV and the pulse repetition rate was adjusted 5 - 100 pulses/sec (pps). The initial ethylene concentration of simulated gas was regulated at 100 ppm; gas flow rate was fixed to 5.0 L/min; and oxygen concentration was changed to 2, 5, 10, and 20%. The ethylene concentrations and by-products such as carbon monoxide (CO), carbon dioxide (CO₂), formic acid (HCOOH), nitrous oxide (N₂O), and nitric acid (HNO₃) in the untreated and treated gases were analyzed by the Fourier Transform Infrared Spectroscopy (FT-IR). Ozone (O₃) was analyzed by Ultraviolet Visible Adsorption Spectrophotometer (UV-VIS). The results show that ethylene was completely decomposed at 40 J/L.

Keywords

Non-thermal plasma, Nanosecond pulsed discharge, ethylene, VOCs, Plasma process.

1. Introduction

Non-thermal plasma has been investigated for gas purification [1], [2], [3], [4], ozone generation using methods such as dielectric barrier discharge (DBD) [5]. However, energy efficiency requires further improvement. Namihira et al. developed a nanosecond pulsed discharge system having higher energy efficiency compared with other discharge methods such as corona discharge and DBD. Fig. 1 shows Characteristics map of NO removal efficiency against NO removal ratio [6]. In Fig. 1, the nanosecond pulsed discharge demonstrates higher NO removal efficiency than other discharge methods.

In the long-term transport of fruits and vegetables, it is a problem that the freshness of fruits and vegetables deteriorates due to ethylene(C₂H₄) released from products [7]. The ethylene, a kind of plant hormone also known as VOCs, has the effect of promoting the growth of fruits and vegetables [7], [8]. The ethylene

released from the products promotes maturation of the fruits and vegetables during long-term transport in a sealed space such as container ship [9], [10]. Therefore, the ethylene concentration should be kept low during transport. Recently, in order to reduce the influence of ethylene, controlled Atmosphere Storage (CA storage) is conducted [11]. The CA storage keeps freshness of products by reducing biological activity of fruits and vegetables such as ethylene release and respiration by adjusting the composition (N₂:80 - 96 %, O₂:2 - 10 %, CO₂:2 - 10 %) and humidity (90 - 95 % of relative humidity) of gas. However, the combination of CA storage with other methods for reducing ethylene is required, because the CA storage cannot completely reduce influence of ethylene. In this research, approximately 100 ppm of ethylene decomposition in various gas composition at room temperature by the nanosecond pulsed discharge were examined. The influence of oxygen concentration (2, 5, 10, 20 %) to

the ethylene removal ratio, efficiency and the generation of by-products were investigated.

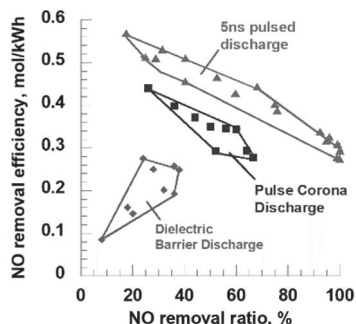


Fig. 1 Characteristic map of NO removal efficiency against NO removal ratio [6].

2. Experimental Setup

2.1 Nanosecond pulse generator

In conventional pulsed discharges by approximately 100 ns of pulse width, it is known that the discharge phase consists of a streamer discharge phase followed by a glow discharge phase [12]. During the glow discharge phase, a temperature rise occurs, which causes energy loss. On the other hand, the nanosecond pulse generator prevents transition to the glow discharge phase because of generating pulsed high voltage with 5 ns of duration (theoretical value) and 2 ns of rise and fall times. The details of nanosecond pulse generator can be found in [6]. Fig. 2 Shows schematic of discharge reactor. The stainless-steel rod 1.0 mm of inner diameter was used as inner electrode applied high voltage. Furthermore, the stainless-steel cylinder 76 mm of inner diameter was used as ground electrode. The length of reactor was 1000 mm. Fig. 3 shows the typical output waveforms, (a) applied voltage, (b) discharge current and (c) input energy to discharge reactor per pulse. As increasing the applied voltage, saturation point of input energy increase.

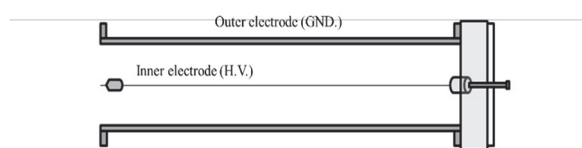
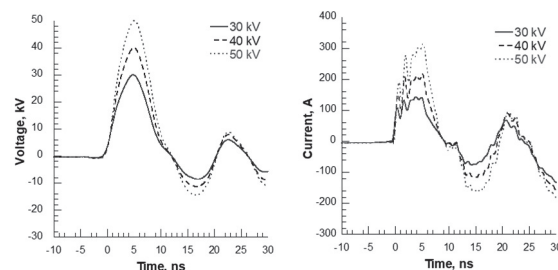
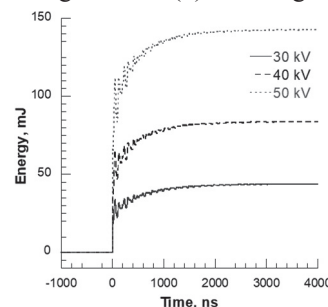


Fig. 2 Schematic of coaxial cylinder type discharge reactor.



(a) Applied voltage.

(b) Discharge current.



(c) Input energy waveform to reactor per pulse.

Fig. 3 Typical output waveforms of nanosecond pulse generator.

For characterization of ethylene removal performance, Input energy densities (IED) are defined by (1);

$$\text{IED, J/L} = \frac{E \times f \times 60}{G} \quad (1)$$

Where E is energy consumed in the reactor per pulse obtained from time integration of the consumed power [W], f is pulse repetition rate [pps], and G is toluene including gas flow rate [L/min], respectively.

2.2 Experimental System

Experimental system for ethylene decomposition is shown in Fig. 4. Ethylene concentration in the nitrogen (N_2) and oxygen (O_2) mixed gas was adjusted at 100 – 110 ppm by controlling the gas mixture ratio. Mixed gas of N_2 (80 - 98 %) and O_2 (20 - 2 %) from gas cylinders was used as sample gas. The gas flow rate fixed at 5.0 L/min by mass flow controllers (KOFLOC 8500, Kojima Instruments, Japan). The mixed gas containing ethylene was fed into discharge reactor. The discharge plasma caused by the nanosecond pulse

voltage occurs in discharge reactor, and ethylene was treated by discharge plasma. In this work, the nanosecond pulse generator was operated under 40 kV of applied voltage to the discharge reactor, at 5 - 100 pps of pulse repetition rate. The untreated and treated gas were introduced into Ultraviolet Visible Adsorption Spectrophotometer (UV-VIS, V-550, JASCO Corporation, Japan) and Fourier Transform Infrared Spectroscopy (FT-IR, IG-1000, Otsuka electronics Co., Japan). The ethylene concentrations and some byproducts such as carbon monoxide (CO), carbon dioxide (CO₂), formic acid (HCOOH), nitrous oxide (N₂O), and nitric acid (HNO₃) in the untreated and treated gases were analyzed by the FT-IR. Furthermore, Ozone (O₃) was analyzed by UV-VIS. The ethylene removal ratio (2) and the ethylene removal efficiency (3) were defined as flow:

Ethylene removal ratio, %

$$= \frac{[C_2H_4]_0 - [C_2H_4]}{[C_2H_4]_0} \quad (2)$$

Ethylene removal efficiency, g/kWh

$$= \frac{G \times M_{ethylene}}{22.4} \times \frac{([C_2H_4]_0 - [C_2H_4])}{f \times E \times 10^{-3} \times \frac{1}{60}} \quad (3)$$

where $[C_2H_4]$ is the ethylene concentration after treatment, $[C_2H_4]_0$ is the ethylene initial concentration, f is the pulse repetition rate, G is the gas flow rate, E is the input energy to discharge reactor per pulse, $M_{ethylene}$ is the ethylene molecular mass, respectively.

3. Results and Discussion

3.1 IR spectrum analysis

Fig. 6 shows the IR spectrum in the case of before and after treatment with 40 kV of applied voltage and 50 pps of pulse repetition ratio corresponding to 40.2 J/L of input energy density. The oxygen concentration was set as 20 %. In Fig. 6, the absorbance peaks at 950 cm⁻¹ correspond to ethylene which decreases at after

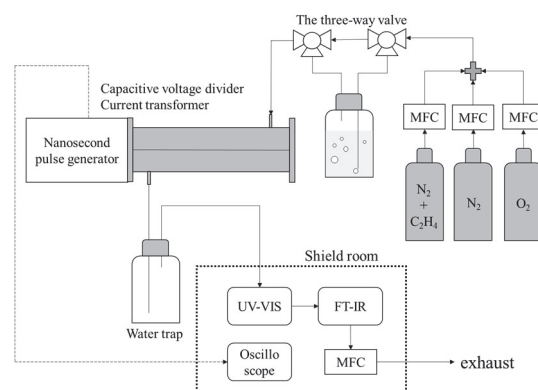
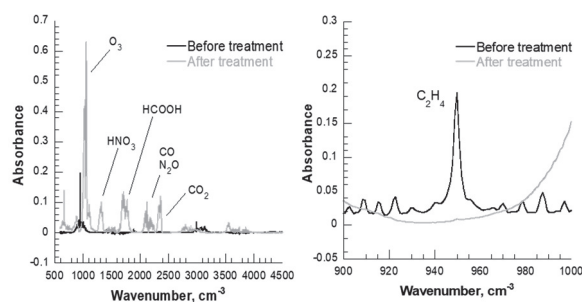


Fig. 4 Schematic of experimental system for ethylene decomposition.

treatment. Furthermore, the by-products such as CO, N₂O, HNO₃, HCOOH, H₂O, O₃ are generated in the decomposition process of ethylene. Therefore, the absorbance peaks corresponding to each by-product were observed in IR spectrum at after treatment.



(a) wide range

(b) narrow range

Fig. 5 FT-IR absorbance spectra before and after treatment

3.2 Characteristics of ethylene decomposition

Fig. 6 shows dependence of ethylene removal ratio on input energy density into the discharge reactor for 2, 5, 10, 20 % (N₂ balance) of O₂ concentration. The total gas flow rate and the applied voltage were 5.0 L/min and 40 kV, respectively. In Fig. 6, the ethylene removal ratio increased with increasing input energy density at each oxygen concentration. Furthermore, ethylene was completely decomposed approximately 40 J/L of input energy density when 5, 10, 20 % of O₂ concentration. On the other hand, the ethylene removal ratio reached 100 % in approximately 50 J/L of input energy density at 2 % of O₂ concentration. Fig. 7

TABLE I By-products generation at different O₂ concentration when ethylene was completely decomposed.

Oxygen Concentration, %	Concentrations of each by-product, ppm					
	CO ₂	N ₂ O	O ₃	CO	HNO ₃	HCOOH
20	22	6	361	96	36	25
10	20	6	263	97	36	23
5	18	7	224	103	39	21
2	16	6	90	99	28	16

shows dependence of ethylene removal efficiency on ethylene removal ratio for different O₂ concentration. In Fig. 7, the ethylene removal efficiency decreases with decreasing oxygen concentration and increasing ethylene removal ratio. In the case of 2 % of O₂ concentration, the ethylene removal efficiency, when ethylene was completely decomposed, was approximately 10 g/kWh. Furthermore, the maximum ethylene removal efficiency was approximately 32 g/m³. These removal efficiencies are higher than the other discharge methods as VOCs treatment method [13]. Table I shows by-products concentration calculated by absorbance peak after treatment on 100 % of ethylene removal ratio at each oxygen concentration. In table I, the O₃ concentration sharply decreased with decreasing oxygen concentration. Especially, the O₃ concentration was 90 ppm at 2 % of O₂ concentration; less than 25 % of synthesis air (N₂: 80 %, O₂: 20 %). Furthermore, CO₂ and HCOOH concentration slightly decreased with decreasing oxygen concentration. On the other hand, the other by-products concentration was hardly affected by oxygen concentration.

4. Conclusions

In this study, characteristics of ethylene decomposition by the nanosecond pulsed discharge was investigated. Results are summarized as follows.

1) The ethylene removal ratio was completely decomposed approximately 40 J/L of input energy density in the synthesis air. The necessary input energy

density for complete decomposition of ethylene was increased with decreasing the O₂ concentration.

2) the O₃ concentration sharply decreased with decreasing oxygen concentration. Especially, the O₃ concentration was 90 ppm at 2 % of O₂ concentration; less than 25 % of synthesis air.

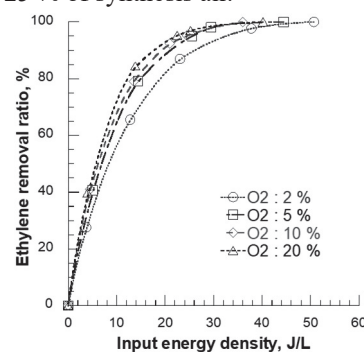


Fig. 6 Dependence of ethylene removal ratio on input energy density under each gas oxygen concentration.

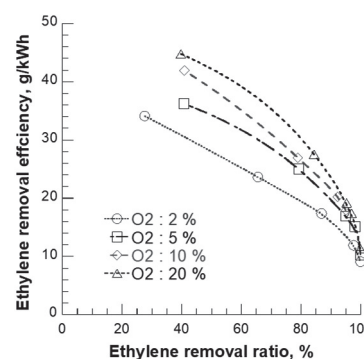


Fig. 7 Dependence of ethylene removal efficiency on ethylene removal ratio under each gas oxygen concentration.

References

- [1] F.J.C.M. Beckers, et al., "Pulsed Corona Demonstrator for Semi-Industrial Scale Air Purification", *IEEE Trans. Plasma Sci.*, Vol. 41, No. 10, (2013).
- [2] F.J.C.M. Beckers et al., "Low-level NO_x removal in ambient air by pulsed corona technology", *J. Phys. D: Appl. Phys.*, Vol. 46 (2013)
- [3] A. Ogasawara et al., "Decomposition of Toluene Using Nanosecond- Pulsed-Discharge Plasma Assisted With Catalysts", *IEEE Trans. Plasma Sci.*, Vol. 43 (2015).
- [4] M. Sanjeeva Gandhi et al., "Time dependence of ethylene decomposition and byproducts formation in a continuous flow dielectric-packed plasma reactor.", *Chemosphere*, 91, pp.685-691 (2013).
- [5] Z. Fang, Y. Qiu, Y. Sun, H. Wang, K. Edmund, "Experimental study on discharge characteristics and ozone generation of dielectric barrier discharge in cylinder-cylinder reactor and a wire-cylinder reactor", *Journal of Electrostatics*, Vol. 66, 2018.
- [6] D. Wang, T. Namihira, H. Akiyama, "Recent Progress of Nano-seconds Pulsed Discharge and its Applications", *J. Adv. Oxid. Technol*, Vol. 14, No. 1, 2011.
- [7] K. Takaki, J. Nishimura, S. Koide, K. Takahashi, T. Uchino, "Decomposition of Ethylene Using Dual-Polarity Pulsed Dielectric Barrier Discharge", *IEEE Trans. Plasma Sci.*, Vol. 43, No. 10, 2015.
- [8] J. Nishimura, K. Takahashi, K. Takaki, S. koide, M. Suga, T. Orikasa, Y. Teramoto, T. Uchino, "Removal of Ethylene and by-products Using Dielectric Barrier Discharge with Ag Nanoparticle-Loaded for Keeping Freshness of Fruits and Vegetables", *Trans. Mat. Res. Soc. Japan*, 41[1], 41-45, 2016.
- [9] K. Takahashi, T. Motodate, K. Takaki, S. Koide, "Influence of oxygen concentration on ethylene removal using dielectric barrier discharge", *Jpn. J. Appl. Phys.* 57, 01AG04, 2018.
- [10] V.I. Golota, D.V. kudin, O.V. Manuilenko, G.V. Taran, L.M. Zavada, M.O. Yegorov, V.F. Khmelevskaya, "Decomposition of ethylene in low temperature plasma of barrierless discharge.", *Problems of Atomic Science and Technology*, No. 4(116), 2018.
- [11] Kimberly Palmer Wright, Adel A. Kader, "Effect of controlled-atmosphere storage on the quality and carotenoid content of sliced persimmons and peach", *Postharvest Biology and Technology*, 10, 89-97, 1997.
- [12] D. Wang, M. Jikuya, S. Yoshida, T. Namihira, S. Katsuki, H. Akiyama, "Positive- and Negative-Pulsed Streamer Discharges Generated by a 100-ns Pulsed-Power in Atmospheric Air", *IEEE Trans. Plasma Sci.*, Vol. 35, No. 4, 2007.
- [13] D. Li, D. Yakushiji, S. Kanazawa, T. Ohkubo, Y. Nomoto, "Decomposition of toluene by streamer corona discharge with catalyst", *Journal of Electrostatics*, 55, 311-319, 2002.

Characteristic Investigation of the Pulsed Radiation Generated by Electron Beam Irradiation

Kenji Kashine^{1*}, Taiki Fujishiro¹, Yusuke Nakayama², Fumihito Tamura³,
Takashi Kikuchi², Weihua Jiang², Akira Tokuchi⁴

1 National Institute of Technology, Kagoshima college (1460-1, Hayato, Kirishima, 899-5193, Japan)*

2 Nagaoka University of Technology (1603-1, Kamitomioka, Nagaoka, 940-2188, Japan)

3 National Institute of Technology, Nagaoka college (888, Nishikatagaimachi, Nagaoka, 940-8532, Japan)

4 Pulsed Power Japan Laboratory Ltd. (4-5-2, Nomura, Kusatsu, 525-0027, Japan)

ABSTRACT

The characteristic investigation of a pulsed radiation which is generated by irradiating an electron beam to aluminum target was performed. An original X-ray detecting device was used for evaluating the power output of pulsed radiation source which is operated by intense pulsed power generator. The calibration equation which is correspondence between an acquired peak voltage to power output of an existing X-ray generating equipment was obtained. We confirmed that the pulsed radiation source has approximately 820 MW of power output for generating the high strength and widespread of pulsed X-ray.

Keywords

Key Words (pulsed X-ray, radiation source, pulsed electron beam)

1. Introduction

When irradiate a pulsed electron beam to a solid target, highly energy is deposited into the target. At an instant, highly temperature and density of plasma has been generated. This unique pulsed plasma has several possibilities for using the variety of applications [1][2].

As one of expected application, there is a pulsed radiation source which radiate X-ray and γ -ray. For widely use of this radiation source, investigating the radiation energy of it is required. However, the intense pulsed electron beam which has accelerating voltage range of mega-volts and its pulse width of under 100 ns can make a large scale of dense plasma. Therefore, because of the intensity of radiation which is radiated from this dense plasma is expected to be extremely high, a normal spectrum analyze is impossible.

In previous study, the radiation energy measurement of a pulsed radiation which is generated by irradiating an electron beam to aluminum target was performed. An NaI(Tl) scintillation detector and a shaping amplifier were used for measuring the radiation energy. From the actual experiment, the radiation energy per unit area was estimated to be 12 MeV/mm² for one shot of electron beam irradiation. Moreover, a CCD camera was used for estimating the radiation areal density. Number of white dots which considerable to effect caused by the radiation were existed in an acquired image. The areal density of white dots was obtained to be approximately 6000 dot/mm² at the behind of 3 m from the radiation source.

For further investigation, we tried to estimate the power output of this pulsed radiation source. In this

paper, we describe methods and equipments for estimating the power output of the pulsed radiation source as a virtual X-ray generator.

2. Experimental Setup

2.1 Pulsed radiation generating device

The intense pulsed power generator named ETIGO-II [3] was used for driving an electron beam diode. The hemispherical shape and strip arranged anode which has curvature radius of 135 mm was used for focusing the electron beam.

Figure 1 shows a typical waveform of the diode voltage and current. The peak voltage and current were -0.9 MV and 80 kA respectively, and its pulse width was approximately 100 ns.

An aluminum board which has 3 mm of thickness was set at the beam focusing point. The electron beam diode and the aluminum target were set into the vacuum chamber which has an acrylic window placed behind the target.

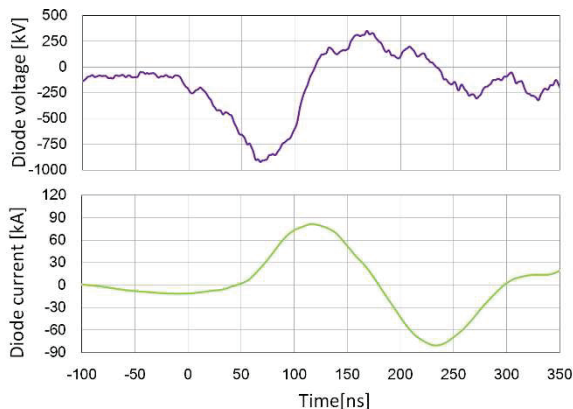


Fig. 1 Voltage and current waveform at the diode section

2.2 X-ray detecting device

An original X-ray detecting device was designed. This device can be acquired the signal which is in proportion to X-ray strength. The calibration equation which is correspondence between a peak value of acquired signal to power output of X-ray generator was obtained by using an existing X-ray generator. By using this device and equation, the power output of the pulsed radiation source which is generated by

irradiating an electron beam to aluminum target was estimated.

Figure 2 shows the circuit diagram of X-ray detecting device. A scintillation detector which is coupled with a scintillator and a photodiode was used. Table 1 shows the configuration of used scintillation detector. 4mm thickness of CsI(Tl) scintillator was used in this detector.

Figure 3 shows the overview of an X-ray detecting device. A 50 mm thickness of lead block which has 10 mm diameter aperture in the center of it was used for covering the scintillation detector.

The detected signal was transmitted using the shielded coaxial cable to oscilloscope. A terminal resistance was set at the end of coaxial cable. The terminal current (I_t) which flow into the terminal resistance was used for evaluating X-ray strength.

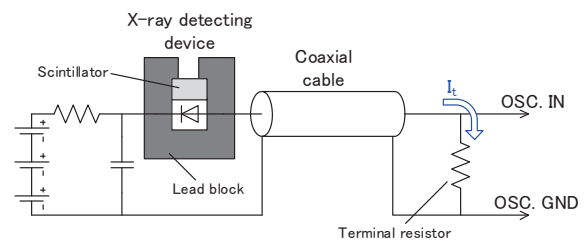


Fig. 2 Circuit diagram of X-ray detecting device

Table 1 Configuration of scintillation detector

Photodiode	First sensor: X100-7 THD
Active area	10 × 10 mm ²
Scintillator	CsI(Tl) 4mm thickness
Detectable radiation	Gamma radiation 1 ~ 10000 keV



Fig. 3 Appearance of X-ray detecting device

2.3 Calibration experiment

Figure 4 shows the layout of calibration experiment.

A 300W class X-ray generator (GE Sensing & Inspection Technologies, ERESKO 160MF4-R) was used for generating various strength of X-ray. A tungsten anode is used in its X-ray tube. The X-ray strength is adjusted by changing its X-ray tube current and voltage. The product of X-ray tube current and voltage was defined the power output of X-ray generator. The X-ray detecting device was set at 40 cm front of the X-ray generator. A 1.2 kΩ of terminal resistance was used in this calibration experiment. The duration of X-ray irradiation was set of 20 second.

Figure 5 shows the typical waveform acquired by the detecting device. In this case, the power output of X-ray was 480W (160 kV × 3 mA). The value of its vertical axis was converted into the terminal current. Various value of spiking signals were appeared in the acquired signal. The average value of this acquired signal was used for evaluating the terminal current on each power output of X-ray generator.

Figure 6 shows the calibration result. The power output was linearly in proportion to the terminal current. By using this result, an arbitrary peak voltage which is acquired by the X-ray detecting device can be translated into the power output of virtual X-ray generator.

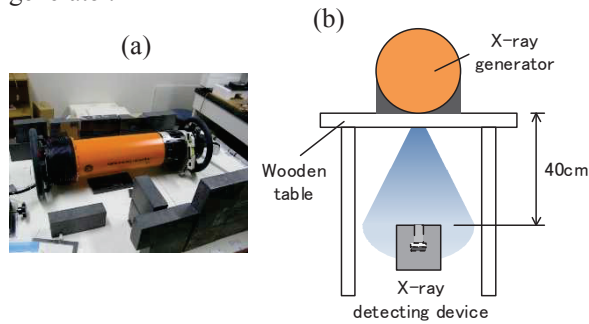


Fig. 4 Outline of the calibration experiment
(a)X-ray generator (b)Experimental setup

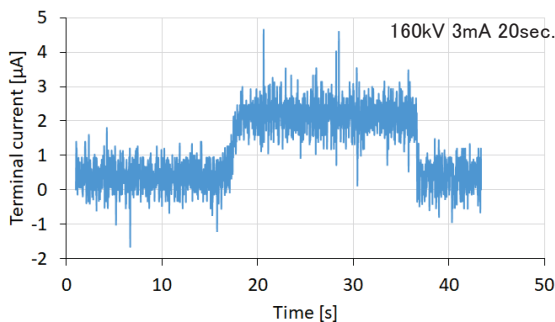


Fig. 5 Acquired waveform of terminal current

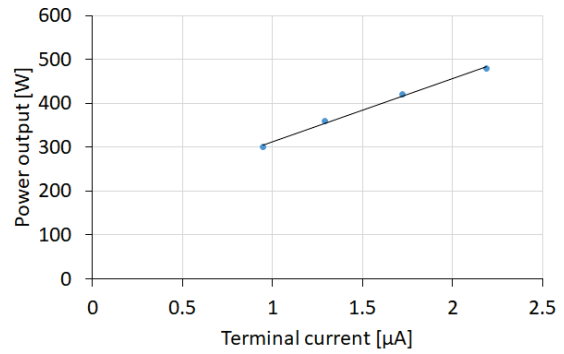


Fig. 6 Dependence of power output on terminal current

3. Results and Discussion

Figure 7 shows experimental setup of X-ray detection at the front of pulsed radiation source. The X-ray detecting device was set behind 4 m from the aluminum target. A 50Ω of terminal resistance was used in this experiment.

Figure 8 shows the acquired waveform at single-pulse of electron beam irradiation. The value of its vertical axis was converted into the terminal current. The noise signal which considerable to be affected by the induced voltage into the electron beam diode was appeared in the acquired signal as shown in Fig.8 (a). In previous study, we confirmed that the diode voltage signal contains above 5000 kHz of frequency. Fig.8 (b) is a filtered waveform that is applied to numerical treatment of low pass filter ($f_c = 5000$ kHz). A peak terminal current of 57 mA was obtained from this result.

In the case of a point radiation source, the radiation emits spherically. Therefore, it is considerable to the areal density of radiation is decrease in inverse proportion to the square of the distance. Dependence of power output on terminal current at 40 cm front of the X-ray generator (Fig.6) is converted into the case of 4 m of distance. The equation of the relationship between the power output (P_o) and terminal current (I_t) was given by follows,

$$P_o [W] = 14385 \times I_t [\mu A] + 168.8 \quad (1)$$

From the result of acquired peak terminal current of 57 mA, approximately 820MW of power output was

obtained. This result suggests that pulsed radiation source which generated by the pulsed electron beam irradiation can be 820MW class of X-ray generator. Moreover, this pulsed radiation source can generate high strength and widespread of pulsed X-ray.

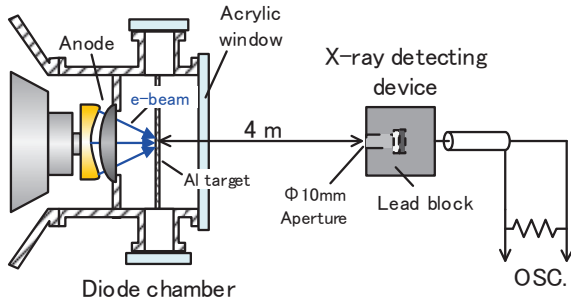


Fig. 7 Schematic of experimental setup

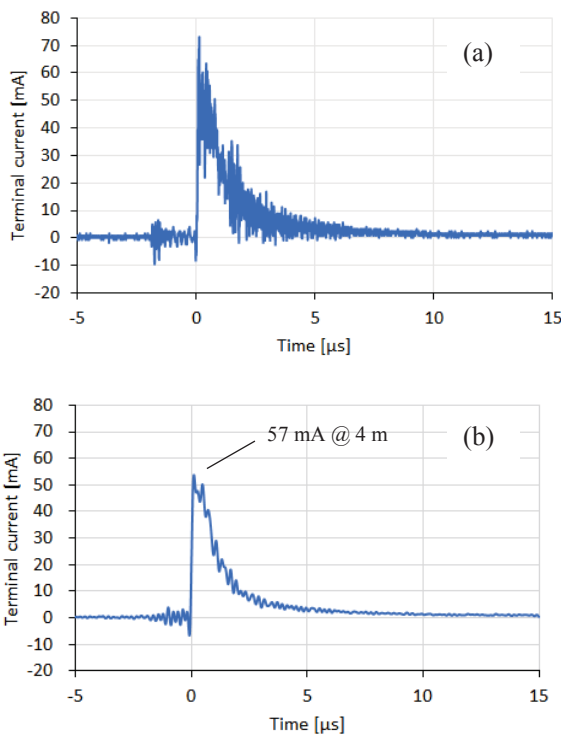


Fig. 8 Acquired waveform of X-ray detecting device
(a) Actual signal (b) Filtered signal

4. Conclusions

In this research, characteristic investigation of a pulsed radiation which is generated by an electron beam irradiation was performed.

An original X-ray detecting device was used for

evaluating the power output of pulsed radiation source which is operated by intense pulsed power generator. The calibration equation which is correspondence between an acquired peak voltage to power output of X-ray generating equipment was obtained in advance. The highly power output was obtained to be 820 MW for one shot of electron beam irradiation.

We confirmed that high strength and widespread of pulsed X-ray can be generated by using the electron beam irradiation.

For decommissioning of Fukushima Daiichi Nuclear Power plant (Fukushima-1), various types of survey robot have been developed. Performance tests under a simulated high radiation dose is essential in designing such robots. Our developed radiation source has a possibility for using the performance test of survey robots which is put into the containment vessel of Fukushima-1.

This work was supported by JSPS KAKENHI Grant-in-Aid for Scientific Research(C) Grant Number 16K06934 and 17K06333.

References

- [1] F. Tamura, R. Hayashi, T. Kudo, A. Watabe, K. Kashine, A. Tokuchi, T. Kikuchi, K. Takahashi, T. Sasaki, T. Aso, Nob. Harada, and W. Jiang, "Concept for Generation of Warm Dense Matter of Insulator due to Flyer Impact Accelerated by Electron Beam Irradiation using Intense Pulsed Power Generator", *J. Phys. Conference Series*, Vol.688, 012121 (2016).
- [2] K. Kashine, T. Kikuchi, T. Sasaki, R. Hayashi, F. Tamura, A. Watabe, T. Kudo, T. Aso, K. Takahashi, Nob. Harada, W. Jiang, and A. Tokuchi, "Recent Progress in the Intense Pulsed Power Generator ETIGO-II", *Transactions on GIGAKU*, 02015/I-6 (2014).
- [3] W. Jiang, T. Sakagami, K. Masugata, and K. Yatsui, "Tight Focusing of Intense Pulsed Light-Ion Beam by Spherical "Plasma Focus Diode"", *Jpn. J. Appl. Phys.*, Vol.32, pp. L752-L754 (1993).